

# A Physical Classification Scheme for Blazars

Hermine Landt<sup>1,2,3</sup>, Paolo Padovani<sup>1,4,5</sup>, Eric S. Perlman<sup>6</sup>, Paolo Giommi<sup>7</sup>

<sup>1</sup> *Space Telescope Science Institute, 3700 San Martin Drive, Baltimore, MD 21218, USA*

<sup>2</sup> *Hamburger Sternwarte, Gojenbergsweg 112, D-21029 Hamburg, Germany*

<sup>3</sup> *Current address: Harvard-Smithsonian Center for Astrophysics, 60 Garden Street, Cambridge, MA 02138, USA*

<sup>4</sup> *Affiliated with the Space Telescope Division of the European Space Agency, ESTEC, Noordwijk, The Netherlands*

<sup>5</sup> *Current address: European Southern Observatory, Karl-Schwarzschild-Str. 2, D-85748 Garching bei München, Germany*

<sup>6</sup> *Joint Center for Astrophysics, University of Maryland, 1000 Hilltop Circle, Baltimore, MD 21250, USA*

<sup>7</sup> *ASI Science Data Center, c/o ESRIN, Via G. Galilei, I-00044 Frascati, Italy*

Accepted , Received

## ABSTRACT

Blazars are currently separated into BL Lacertae objects (BL Lacs) and flat spectrum radio quasars (FSRQ) based on the strength of their emission lines. This is done rather arbitrarily by defining a diagonal line in the Ca H&K break value – equivalent width plane, following Marchã et al. We readdress this problem and put the classification scheme for blazars on firm physical grounds. We study  $\sim 100$  blazars and radio galaxies from the Deep X-ray Radio Blazar Survey (DXRBS) and 2 Jy radio survey and find a significant bimodality for the narrow emission line [O III]  $\lambda 5007$ . This suggests the presence of two physically distinct classes of radio-loud AGN. We show that all radio-loud AGN, blazars and radio galaxies, can be effectively separated into weak- and strong-lined sources using the [O III]  $\lambda 5007$  – [O II]  $\lambda 3727$  equivalent width plane. This plane allows one to disentangle orientation effects from intrinsic variations in radio-loud AGN. Based on DXRBS, the strongly beamed sources of the new class of weak-lined radio-loud AGN are made up of BL Lacs at the  $\sim 75$  per cent level, whereas those of the strong-lined radio-loud AGN include mostly ( $\sim 97$  per cent) quasars.

**Key words:** galaxies: active - quasars: emission lines - BL Lacertae objects: general

## 1 INTRODUCTION

BL Lacertae objects (BL Lacs) and flat spectrum radio quasars (FSRQ), commonly referred to as blazars, are the most extreme variety of active galactic nuclei (AGN) known. Their signal properties include irregular and rapid variability, high radio and optical polarization, a core-dominated radio morphology, flat ( $\alpha_r \lesssim 0.5$ , where  $S_\nu \propto \nu^{-\alpha}$ ) radio spectra, apparent superluminal motion, and a broad continuum extending from the radio through the gamma-rays.

The properties of blazars can be best explained if we assume that we view in fact a relativistic jet pointed close to our line of sight (as originally proposed by Blandford & Rees 1978). In this scenario the large population of misdirected blazars, i.e., the so-called ‘parent population’, is formed by the classical double-lobed radio galaxies. In particular, low-luminosity radio galaxies (Fanaroff-Riley type I [FR I]; Fanaroff & Riley 1974) appear to be the parent population of BL Lacs (Padovani & Urry 1990,

1991; Urry et al. 1991), while high-luminosity radio galaxies (Fanaroff-Riley type II [FR II]) are believed to be viewed mainly as FSRQ when their jets are pointed close to our line of sight (Padovani & Urry 1992; Urry & Padovani 1995).

Blazars are currently separated into BL Lacs and FSRQ based on the strength of their emission lines. This quantitative distinction between blazar subclasses was prompted by observations of variable weak emission lines in BL Lacs, which had been previously defined as compact, radio-loud AGN with completely featureless optical spectra (Strittmatter et al. 1972). A first (and rather arbitrary) limit on the strength of BL Lac emission lines was introduced by surveys that selected the first complete samples of these objects, namely the 1 Jy radio survey (Stickel et al. 1991) and the *EINSTEIN* Medium Sensitivity Survey (EMSS) at X-ray frequencies (Stocke et al. 1991). Both these surveys chose a value of 5 Å for the maximum equivalent width of BL Lac emission lines (applied to the rest and observer’s frame respectively).

The 1 Jy survey and EMSS also introduced the first quantitative separation between blazars and radio galaxies. The 1 Jy survey used for this purpose the radio spectral index and defined BL Lacs and radio galaxies as sources with  $\alpha_r \leq 0.5$  and  $\alpha_r > 0.5$  respectively. The EMSS, on the other hand, did not use radio information to classify its objects (since it searched also for radio-quiet BL Lacs, which could not be found), and introduced the value of the Ca H&K break (a stellar absorption feature) as an additional criterion. A maximum Ca H&K break value of 25 per cent was adopted for BL Lacs in order to ensure the presence of a substantial non-thermal jet continuum in addition to the thermal spectrum of the elliptical host galaxy.

The Ca H&K break limit separating blazars and radio galaxies, as well as the equivalent width limit separating BL Lacs and FSRQ were later revised by Marchã et al. (1996). These authors argued that any radio-loud AGN with a Ca H&K break below 40 per cent (and not only below 25 per cent) should be classified as a blazar, and proposed a diagonal line in the Ca H&K break value – equivalent width plane (see Fig. 1) to separate BL Lacs (left of the line) and quasars (right of the line). This diagonal line was the result of simulations for only one object, 3C 371, which was chosen on the grounds that it was widely accepted as a ‘genuine’ BL Lac. Subsequently, Scarpa & Falomo (1997) showed that there was a continuity in optical continuum and Mg II  $\lambda 2798$  luminosity between BL Lacs and FSRQ and argued against the existence of two populations of blazars from the point of view of emission line strengths.

The rather arbitrary separation of blazars proposed by Marchã et al. and the results of Scarpa and Falomo make the revision of blazar classification highly necessary. Such a revision is of particular interest at this time since several relatively large blazar surveys are being identified, e.g., RGB (*ROSAT* All Sky Survey RASS-Green Bank; Laurent-Muehleisen et al. 1998, 1999), REX (Radio-Emitting X-ray sources; Caccianiga et al. 1999, 2000), the Sedentary Survey (Giommi et al. 1999), CLASS (Cosmic Lens All Sky Survey) blazar sample (Marchã et al. 2001; Caccianiga et al. 2002), and DXRBS (Deep X-ray Radio Blazar Survey; Perlman et al. 1998; Landt et al. 2001). In this paper, we use an homogeneous sample of blazars from DXRBS, i.e., a sample selected in a uniform and therefore presumably unbiased way, to devise a physically based classification scheme. DXRBS is most suitable for a physical revision of blazar classification since it contains a large number of objects ( $\sim 350$ ) and includes both types of blazars, BL Lacs and FSRQ. Moreover, measurements are available on several emission line parameters as well as on multiwavelength continuum properties.

The paper is organized as follows. In Sections 2 and 3 we present our sample of objects and describe the emission line measurements. In Section 4 we discuss the current blazar classification scheme proposed by Marchã et al. and show its limitations. In Section 5 we introduce a (new) physical classification scheme for blazars. In Sections 6 and 7 we discuss our results and present our conclusions. Throughout this paper we have assumed cosmological parameters  $H_0 = 50$  km

$s^{-1}$  Mpc $^{-1}$  and  $q_0 = 0$ . Spectral indices have been defined as  $S_\nu \propto \nu^{-\alpha}$ .

## 2 THE SAMPLES

We have selected for our analysis sources from the Deep X-ray Radio Blazar Survey (DXRBS). DXRBS is the result of a cross-correlation of all serendipitous X-ray sources in the publicly available *ROSAT* database WGACAT (first revision: White et al. (1995)) with a number of publicly available radio catalogs (the 20 cm and 6 cm Green Bank survey catalogs NORTH20CM and GB6 for the northern part of the sky, and the 6 cm Parkes-MIT-NRAO catalog PMN for the southern part of the sky). All sources with radio spectral index  $\alpha_r \leq 0.7$  at a few GHz and off the Galactic plane ( $|b| > 10^\circ$ ) have been selected as blazar candidates. For a detailed description of the selection and identification procedures of the DXRBS see Perlman et al. (1998) and Landt et al. (2001). As of June 2003 the DXRBS complete sample is  $\sim 95$  per cent identified. We have initially classified sources in our sample following the scheme proposed by Marchã et al. (1996) and described in Section 4. The total sample (which includes also 22 ‘low priority sources’, i.e., sources that do not meet all selection criteria) contains 341 objects: 261 quasars (201 flat spectrum radio quasars [ $\alpha_r \leq 0.5$ ] and 60 steep spectrum radio quasars [ $\alpha_r > 0.5$ ]), 44 BL Lacs, and 36 radio galaxies.

We have selected all DXRBS BL Lacs, but have restricted the sample of FSRQ to objects with redshifts  $z \leq 2.2$ . This was done in order to compare BL Lacs and FSRQ that have the same emission lines. The strongest emission lines common to both were Mg II  $\lambda 2798$ , [O II]  $\lambda 3727$ , H $\beta$   $\lambda 4861$ , [O III]  $\lambda 5007$ , and H $\alpha$   $\lambda 6563$ . Then,  $z \sim 2.2$  represents the maximum redshift for which Mg II can be observed in the  $\sim 4000 - 9000$  Å range typically covered by our optical spectra.

### 2.1 The BL Lacertae Objects (BL Lacs)

We have an optical spectrum for 28 of the 44 DXRBS BL Lacs (16 objects were previously known sources). Additionally, we could find in the literature information on emission lines for one more source (4C 55.17). Out of the 28 BL Lacs observed by us 5 objects do not have a determined redshift and have been excluded from our analysis. Therefore, the BL Lac sample under study includes 24 objects and is listed in Table 1.

### 2.2 The Flat-Spectrum Radio Quasars (FSRQ)

We have an optical spectrum for 107 of the 178 DXRBS FSRQ with redshifts  $z \leq 2.2$  (71 objects were previously known sources). Out of these we have included in our analysis 91 objects. We have excluded objects that: 1. had a spectrum whose wavelength range did not cover the location of any of the emission lines analyzed here (6 objects); 2. had a spectrum covering the location of Mg II  $\lambda 2798$  only, but either the signal-to-noise ratio (S/N) was below 3 (4

**Table 1.** DXRBS BL Lacs

Name	z	MgII		[OII]		H $\beta$		[OIII]		H $\alpha$		$L_{\text{NLR}}$ [erg/s]	$L_{\text{BLR}}$ [erg/s]	C	$\sigma$
		$W_{\lambda}$ [Å]	log L [erg/s]	$W_{\lambda}$ [Å]	log L [erg/s]	$W_{\lambda}$ [Å]	log L [erg/s]	$W_{\lambda}$ [Å]	log L [erg/s]	$W_{\lambda}$ [Å]	log L [erg/s]				
(1)	(2)	(3)	(4)	(5)	(6)	(7)	(8)	(9)	(10)	(11)	(12)	(13)	(14)	(15)	(16)
WGAJ0023.6+0417	0.100					< 9.8	<39.56	< 7.0	<39.43	<16.4	<39.82	<40.81	<40.76		
WGAJ0032.5–2849	0.324					< 1.6	<41.36						<42.76	0.22	0.08
WGAJ0043.3–2638	1.002	6.5	43.50	< 0.6	<42.28	7.5	43.01					<43.71	44.61	0	
WGAJ0100.1–3337	0.875	10.1	42.71										43.93		
WGAJ0245.2+1047	0.070			15.0	41.08	< 2.3	<40.72	20.6	41.67	20.6	41.65	42.50	42.50	0.26	0.08
WGAJ0313.9+4115	0.029					< 1.7	<40.12	1.9	40.24	19.4	41.17	41.37	42.03	0.38	0.12
WGAJ0428.8–3805	0.150			< 1.9	<40.19	< 1.7	<40.50	< 1.1	<40.32	< 2.2	<40.66	<41.37	<41.64	0.32	0.05
WGAJ0431.9+1731	0.143					< 9.8	<39.97	< 4.7	<39.70	<13.3	<40.20	<40.99	<41.15		
WGAJ0528.5–5820	0.254					< 2.2	<40.81	12.0	41.55			42.40	<42.21	0.38	0.18
WGAJ0533.6–4632	0.332					< 2.4	<40.71						<42.11	0.32	0.15
WGAJ0558.1+5328	0.036					< 2.7	<40.35	8.7	40.84	11.6	41.05	41.82	41.91	0.29	0.16
WGAJ0624.7–3230	0.252			< 2.2	<40.87	< 2.0	<41.05	< 2.0	<41.07	< 6.5	<41.49	<42.08	<42.37	0.22	0.05
WGAJ0816.0–0736	0.040			< 5.0	<39.85	< 2.5	<39.93	< 1.2	<39.63	< 2.2	<39.92	<40.92	<40.98	0.37	0.18
WGAJ0847.2+1133	0.199			< 1.1	<40.35	< 2.2	<40.50	< 1.8	<40.40	< 7.3	<40.76	<41.50	<41.70	0	
WGAJ1204.2–0710	0.185					< 4.5	<41.58	5.1	41.71			42.54	<42.98		
WGAJ1311.3–0521	0.160			< 2.7	<40.50	< 1.6	<40.60	< 1.2	<40.47	< 1.9	<40.63	<41.62	<41.67	0.33	0.12
WGAJ1320.4+0140	1.235	15.2	43.01										44.24		
WGAJ1744.3–0517	0.310			< 3.5	<40.60	< 3.3	<40.72	< 2.6	<40.62			<41.74	<42.12	0.20	0.09
WGAJ1834.2–5948	0.435			<13.0	<40.86	<12.2	<40.84	< 8.0	<40.68			<41.94	<42.24	0.16	0.36
WGAJ1840.9+5452	0.646	<15.3	<42.83	5.5	42.38	< 8.1	<42.53	10.9	42.63			43.61	<44.00	0.06	0.12
WGAJ1936.8–4719	0.264			< 0.5	<40.79	< 0.9	<41.04	< 0.9	<40.95			<41.98	<42.44	0	
WGAJ2258.3–5525	0.479	1.4	41.90	< 0.8	<41.48	< 3.2	<41.95	< 1.7	<41.67			<42.68	43.11	0	
WGAJ2330.6–3724	0.279			0.8	40.18	< 1.4	<40.45	2.4	40.63			41.52	<41.85	0.10	0.04
4C55.17 <sup>a</sup>	0.909	2.8	43.39	1.3	42.92	8.2	43.62	17.6	43.95			44.68	44.77		

Columns: (1) object name, (2) redshift, (3) and (4) Mg II  $\lambda$ 2798, (5) and (6) [O II]  $\lambda$ 3727, (7) and (8) H $\beta$   $\lambda$ 4861, (9) and (10) [O III]  $\lambda$ 5007, (11) and (12) H $\alpha$   $\lambda$ 6563 rest frame equivalent widths and line luminosities respectively, (13) narrow line region luminosity, (14) broad line region luminosity, (15) Ca H&K break value (measured in spectra  $f_{\lambda}$  versus  $\lambda$ ), (16)  $1\sigma$  error on Ca H&K break value

References for emission line data: (a) Lawrence et al. (1996)

objects) or telluric A band was present (2 objects) in that region; 3. had a spectrum that was not taken at parallactic angle and the loss in flux at the location of all emission lines under study was larger than 30 per cent (4 objects; see Section 3 for more details). We note that none of these cases applied to our sample of BL Lacs. Additionally, we could find in the literature information on emission lines for 15 of the previously known sources. The FSRQ sample under study includes 106 objects and is listed in Table 2.

### 2.3 The Steep-Spectrum Radio Quasars (SSRQ)

For our studies in Section 4.2 we have additionally selected DXRBS SSRQ with redshifts  $z \leq 1.2$ , the maximum redshift at which the Ca H&K break is observable in our spectra (40 objects). We have an optical spectrum for 32 sources (8 objects were previously known) and included all of these in our analysis. Additionally, we could find in the literature information on emission lines for two more sources. The SSRQ sample under study includes 34 objects and is listed in Table 3.

### 2.4 The Radio Galaxies

For our studies in Section 4.2 we have additionally selected DXRBS radio galaxies (36 objects). We have an optical spectrum for 18 sources (18 objects were previously known), but have excluded from our analysis 8 objects with no emission lines and a spectrum with a resolution too low to allow for a derivation of non-detection limits (see Section 3 for more details). The sample of radio galaxies under study includes 10 objects and is listed in Table 4.

## 3 EMISSION LINE MEASUREMENTS

Tables 1 to 4 list the rest frame equivalent widths and line luminosities for Mg II  $\lambda$ 2798, [O II]  $\lambda$ 3727, H $\beta$   $\lambda$ 4861, [O III]  $\lambda$ 5007, and H $\alpha$   $\lambda$ 6563 for our sample of DXRBS sources.

In the individual spectra a cubic spline was first fitted interactively to the continuum over the full wavelength range covered using the IRAF task *noao.onedspec.sfit*. The equivalent widths ( $W_{\lambda}$ ) and line fluxes were then measured

**Table 2.** DXRBS FSRQ with  $z \leq 2.2$ 

Name	$z$	MgII		[OII]		H $\beta$		[OIII]		H $\alpha$		$L_{\text{NLR}}$ [erg/s]	$L_{\text{BLR}}$ [erg/s]	C	$\sigma$
		$W_\lambda$ [Å]	log L [erg/s]	$W_\lambda$ [Å]	log L [erg/s]	$W_\lambda$ [Å]	log L [erg/s]	$W_\lambda$ [Å]	log L [erg/s]	$W_\lambda$ [Å]	log L [erg/s]				
(1)	(2)	(3)	(4)	(5)	(6)	(7)	(8)	(9)	(10)	(11)	(12)	(13)	(14)	(15)	(16)
WGAJ0010.5–3027	1.190	55.7	44.16										45.25		
WGAJ0012.5–1629	0.151					22.6	41.87	14.8	41.69	145.1	42.42	42.52	43.26	0.21	0.18
WGAJ0029.0+0509	1.633	41.4	44.49										45.68		
WGAJ0106.7–1034	0.469			9.5	42.53	138.2	43.47					43.96	44.87	0	
WGAJ0110.5–1647	0.781	34.8	44.20	< 3.1	<42.85							<44.28	45.41	0	
WGAJ0126.2–0500	0.411	89.3	42.68	17.7	41.87	36.1	42.00	62.4	42.21			43.15	43.76	0	
WGAJ0136.0–4044	0.649	87.3	42.78	8.5	41.78							43.21	43.99		
WGAJ0143.2–6813	1.223	101.7	43.56										44.71		
WGAJ0217.7–7347	1.234	93.1	43.99										45.13		
WGAJ0253.3+0006	1.339	53.9	42.65										43.86		
WGAJ0258.6–5052	0.834	191.9	42.63	4.9	41.65	<21.6	<42.18					43.09	43.85	0.09	0.16
WGAJ0259.4+1926	0.544	157.4	43.18	6.5	41.70	79.7	42.63	36.3	42.27			43.11	44.25	0	
WGAJ0304.9+0002	0.563	74.9	43.62	2.6	42.01	35.8	42.76	62.1	42.98			43.72	44.65	0	
WGAJ0312.3–6610	1.384	50.3	43.37										44.53	0	
WGAJ0314.4–6548	0.636	106.4	43.54	< 1.9	<41.63	56.9	42.97	11.6	42.28			<43.09	44.59	0	
WGAJ0322.1–5205	0.416					115.8	43.21	25.4	42.59	615.1	43.69	43.33	44.56	0	
WGAJ0322.2–5042	0.651	66.6	43.34	< 2.3	<41.66	69.1	42.91	27.9	42.44			<43.22	44.47	0	
WGAJ0322.6–1335	1.468	93.2	43.44										44.61	0	
WGAJ0357.6–4158	1.271	115.4	43.83										45.03		
WGAJ0411.0–1637	0.622	49.3	44.39	0.6	42.30	28.4	43.41	8.6	42.81			43.67	45.43	0	
WGAJ0427.2–0756	1.375	88.4	44.07										45.77		
WGAJ0435.1–0811	0.791	105.5	43.74	1.7	41.69	35.7	42.46	55.3	42.50			43.27	44.76	0	
WGAJ0441.8–4306	0.872	127.7	42.46	19.8	41.74							43.17	43.67	0	
WGAJ0447.9–0322	0.774	52.4	44.85	1.1	42.97			4.5	43.05			44.13	46.06	0	
WGAJ0448.6–2203	0.496	127.0	42.03	39.4	41.39							42.82	43.24	0	
WGAJ0510.0+1800	0.416	55.8	42.95	5.7	42.18							43.61	44.09	0.02	0.05
WGAJ0535.1–0239	1.033	83.1	44.30										45.58	0	
WGAJ0539.0–3427	0.263					263.7	41.91			169.4	41.82		42.92	0.40	0.22
WGAJ0546.6–6415	0.323			0.8	42.08	93.0	43.84	24.9	43.25	442.2	44.28	43.96	45.15	0	
WGAJ0600.5–3937	1.661	20.7	44.25										45.62		
WGAJ0631.9–5404	0.193			4.2	41.82	77.1	42.96	33.5	42.59	378.0	43.50	43.37	44.34	0	
WGAJ0648.2–4347	1.029	56.7	44.45										45.61	0	
WGAJ0724.3–0715	0.271			< 4.6	<42.05			10.2	42.29	38.6	42.57	<43.28	43.43	0.01	0.15
WGAJ0744.8+2920	1.168	15.2	44.36										45.57	0	
WGAJ0747.0–6744	1.025	85.9	43.47										44.68		
WGAJ0748.2–5257	1.802	37.8	44.69										45.91		
WGAJ0751.0–6726	1.237	42.9	44.33	< 1.6	<42.64							<44.07	45.57		
WGAJ0927.7–0900	0.254					44.7	42.05	24.7	41.77	173.1	42.37	42.59	43.29		
WGAJ0937.2+5008	0.275			< 1.2	<41.29	7.8	42.05	2.4	41.51	30.6	42.25	<42.51	43.25	0	
WGAJ0954.4–0503	0.660	31.9	41.39	10.8	41.20	<16.3	<41.70	10.8	41.51			42.46	42.61	0.32	0.15
WGAJ1003.9+3244	1.682	33.6	44.23										45.68		
WGAJ1006.5+0509	1.216	177.8	43.32										44.67		
WGAJ1010.8–0201	0.896	64.4	43.88			76.0	43.45	23.2	42.90			43.73	45.12		
WGAJ1011.5–0423	1.588	32.8	44.40										45.68		
WGAJ1025.9+1253	0.663	70.4	43.52	2.4	42.01	22.9	42.57	23.5	42.52			43.38	44.51	0	
WGAJ1026.4+6746	1.181	124.7	45.12	< 5.0	<43.33							<44.76	46.33	0	
WGAJ1028.5–0236	0.476	14.9	42.38			< 4.3	<41.83	4.1	41.79			42.60	43.59	0.03	0.02
WGAJ1032.1–1400	1.039	63.8	43.86										45.07		
WGAJ1035.0+5652	0.577	90.0	42.88	< 4.2	<41.51	<32.0	<42.10	< 8.0	<41.53			<42.65	44.09	0	
WGAJ1101.8+6241	0.663			7.8	42.97	43.3	43.30	40.3	43.25			44.22	44.72	0	
WGAJ1104.8+6038	1.373	72.1	44.61	< 6.1	<43.05							<44.48	45.82		
WGAJ1105.3–1813	0.578	50.7	43.40	< 2.5	<41.79	31.7	42.61	17.7	42.32			<43.17	44.42	0	
WGAJ1112.5–3745	0.979	92.0	44.24	3.0	42.57							44.00	45.35	0	
WGAJ1206.2+2823	0.708	62.1	43.44	< 3.1	<41.98							<43.41	44.65	0	
WGAJ1213.2+1443	0.714	179.7	43.69	< 6.1	<42.05			66.5	42.75			<43.55	44.90	0	
WGAJ1217.1+2925	0.974	62.8	43.32	44.6	42.52							43.95	44.54	0	
WGAJ1223.9+0650	1.189	43.9	43.59										44.74		

Table 2 – continued

Name	z	MgII		[OII]		H $\beta$		[OIII]		H $\alpha$		$L_{\text{NLR}}$ [erg/s]	$L_{\text{BLR}}$ [erg/s]	C	$\sigma$
		$W_{\lambda}$ [Å]	log L [erg/s]	$W_{\lambda}$ [Å]	log L [erg/s]	$W_{\lambda}$ [Å]	log L [erg/s]	$W_{\lambda}$ [Å]	log L [erg/s]	$W_{\lambda}$ [Å]	log L [erg/s]				
(1)	(2)	(3)	(4)	(5)	(6)	(7)	(8)	(9)	(10)	(11)	(12)	(13)	(14)	(15)	(16)
WGAJ1300.7–3253	1.256	61.2	44.12	< 4.1	<42.70							<44.13	45.33		
WGAJ1306.6–2428	0.666	109.8	42.52	10.2	41.43	63.0	42.15	54.0	42.07			42.89	43.62	0.03	0.13
WGAJ1314.0–3304	0.484		>43.34*	26.3	42.35	<12.9	<42.03	103.8	42.89			43.74	>44.55*	0.05	0.15
WGAJ1315.1+2841	1.576	24.5	44.35										45.56		
WGAJ1324.0–3623	0.739	47.2	44.18	2.3	42.72	76.5	43.93	27.0	43.47			44.25	45.37	0	
WGAJ1359.6+4010	0.407			4.3	41.79	11.4	42.34	12.8	42.39	150.0	43.22	43.22	44.02	0.13	0.16
WGAJ1416.4+1242	0.335			< 1.9	<41.63	67.4	42.83	21.0	42.32			<43.12	44.23	0	
WGAJ1442.3+5236	1.800	222.9	44.67										45.90		
WGAJ1506.6–4008	1.031	45.8	44.25										45.53	0	
WGAJ1509.5–4340	0.776	40.5	43.94	< 1.6	<42.30	85.6	43.67	20.8	43.06			<43.84	45.12	0	
WGAJ1525.3+4201	1.189	73.6	44.30	< 2.5	<42.78							<44.21	45.51		
WGAJ1543.6+1847	1.396	45.1	44.13										45.38		
WGAJ1606.0+2031	0.383			25.3	41.64	<18.6	<41.70	15.2	41.71	117.9	42.56	42.80	43.42	0.24	0.24
WGAJ1610.3–3958	0.518	25.0	43.04	< 1.3	<41.72	18.5	42.84					<43.15	44.25	0	
WGAJ1629.7+2117	0.833	103.7	43.20	28.9	42.40							43.83	44.41	0	
WGAJ1656.6+5321	1.555	54.0	44.25										45.47		
WGAJ1656.6+6012	0.623	100.4	43.76	4.9	42.23	35.1	42.98	17.3	42.67			43.56	44.79	0	
WGAJ1804.7+1755	0.435	73.2	43.73	< 3.6	<42.24	44.6	43.09	46.7	43.09			<43.85	44.75	0	
WGAJ1808.2–5011	1.606	8.1	43.55										45.43		
WGAJ1826.1–3650	0.888	28.1	43.48										44.69		
WGAJ1827.1–4533	1.244	64.2	44.60										45.77		
WGAJ1911.8–2102	1.420	14.5	43.80										45.22		
WGAJ1938.4–4657	0.805	48.8	41.70	14.4	41.34							42.77	42.91	0.28	0.15
WGAJ2109.7–1332	1.226	69.6	44.75	< 5.0	<43.41							<44.84	45.96		
WGAJ2154.1–1502	1.208	39.4	44.87	< 1.4	<43.17							<44.60	46.28		
WGAJ2157.7+0650	0.625			39.4	42.18	132.9	42.69	187.1	42.83			43.65	44.09	0	
WGAJ2304.8–3624	0.962	139.1	43.12	23.5	42.36							43.79	44.33	0	
WGAJ2320.6+0032	1.894	61.9	43.52										45.49		
WGAJ2322.0+2113	0.707	45.1	44.18	< 1.6	<42.55			12.3	42.73			<43.75	45.40		
WGAJ2329.0+0834	0.948	70.3	43.05										44.26		
WGAJ2333.2–0131	1.062	90.7	43.86										44.94		
WGAJ2349.9–2552	0.844	108.5	43.74	6.0	42.34							43.78	44.95	0	
WGAJ2354.2–0957	0.989	57.8	42.76	12.1	42.02							43.45	43.97	0	
1Jy 0112–017 <sup>a</sup>	1.381	21.0	43.68										44.98		
1Jy 0119+041 <sup>b,c</sup>	0.637	36.0	43.82				43.25		42.80			43.63	44.87		
1Jy 0514–459 <sup>d</sup>	0.194					6.7	42.33	5.0	42.18	35.2	43.00	42.95	43.83		
1Jy 0850+581 <sup>e</sup>	1.322	60.1	45.20	1.1	43.15							44.58	46.34		
1Jy 0859+470 <sup>e</sup>	1.462	73.9	44.84	3.3	43.20							44.64	46.07		
1Jy 1637+574 <sup>e</sup>	0.750	19.9	44.39	1.8	43.04		44.57	11.6	43.72			44.52	45.79		
1Jy 1638+398 <sup>f</sup>	1.666	2.3	43.39										44.65		
1Jy 1725+044 <sup>g</sup>	0.293						43.23		42.15		43.82	42.93	44.67		
1Jy 2344+092 <sup>a</sup>	0.673	41.2	44.62		42.92		44.45					44.36	45.99		
S5 0743+74 <sup>d</sup>	1.629	12.6	44.19										45.40		
S5 1027+74 <sup>h</sup>	0.123			3.6	40.46	39.2	41.91	49.9	42.01		42.37	42.69	43.20		
3C 345 <sup>e</sup>	0.594	55.6	44.86	0.6	42.58		43.23	5.4	43.48			44.23	45.95		
4C 38.41 <sup>e</sup>	1.814	29.3	45.15										46.67		
PKS 2059+034 <sup>a</sup>	1.013	34.3	44.26										45.49		
OY–106 <sup>f</sup>	0.618	17.9	43.19	9.3	42.84			38.3	43.39			44.24	44.40		

Columns: (1) object name, (2) redshift, (3) and (4) Mg II  $\lambda$ 2798, (5) and (6) [O II]  $\lambda$ 3727, (7) and (8) H $\beta$   $\lambda$ 4861, (9) and (10) [O III]  $\lambda$ 5007, (11) and (12) H $\alpha$   $\lambda$ 6563 rest frame equivalent widths and line luminosities respectively, (13) narrow line region luminosity, (14) broad line region luminosity, (15) Ca H&K break value (measured in spectra  $f_{\lambda}$  versus  $\lambda$ ), (16)  $1\sigma$  error on Ca H&K break value

References for emission line data: (a) Baldwin et al. (1989), (b) Richstone & Schmidt (1980), (c) Jackson & Browne (1991), (d) Stickel et al. (1993), (e) Lawrence et al. (1996), (f) Stickel et al. (1989), (g) Jackson & Eracleous (1995), (h) Stickel & Kühr (1993)

\* lower limit since flux loss due to atmospheric differential refraction > 30 per cent

**Table 3.** DXRBS SSRQ with  $z \leq 1.2$ 

Name	$z$	MgII		[OII]		H $\beta$		[OIII]		H $\alpha$		$L_{\text{NLR}}$	$L_{\text{BLR}}$	C	$\sigma$
		$W_\lambda$ [Å]	log L [erg/s]	$W_\lambda$ [Å]	log L [erg/s]	$W_\lambda$ [Å]	log L [erg/s]	$W_\lambda$ [Å]	log L [erg/s]	$W_\lambda$ [Å]	log L [erg/s]				
(1)	(2)	(3)	(4)	(5)	(6)	(7)	(8)	(9)	(10)	(11)	(12)	(13)	(14)	(15)	(16)
WGAJ0034.4–2133	0.764	108.8	42.66	20.4	42.06							43.50	43.88	0.24	0.18
WGAJ0211.9–7351	0.789	48.6	43.33	< 1.5	<41.69							<43.12	44.54	0	
WGAJ0251.9–2051	0.761		>43.79*	0.7	41.74							43.17	>45.01*	0	
WGAJ0307.7–4717	0.599	120.1	43.28	6.9	41.93							43.36	44.49	0.05	0.10
WGAJ0321.6–6641	0.546	54.3	43.27	9.1	42.24	119.0	43.03	143.6	43.05			43.82	44.46	0	
WGAJ0325.0–4927	0.259					43.7	42.47			199.4	42.99		43.84	0	
WGAJ0355.6–1026	0.965	186.8	43.42	13.2	42.15	< 31.8	<42.34	97.2	42.71			43.55	44.53	0	
WGAJ0414.0–1224	0.569	51.0	43.46			106.4	43.30	39.5	42.85			43.68	44.69	0	
WGAJ0414.0–1307	0.463			67.7	42.10							43.53	43.60	0.38	0.21
WGAJ0518.2+0624	0.891	57.6	44.28										45.49		
WGAJ0533.7–5817	0.757	87.1	44.02	4.0	42.43							43.86	45.23	0	
WGAJ0646.8+6807	0.927	79.9	44.39	8.8	43.05							44.49	45.60	0	
WGAJ0829.5+0858	0.866	120.0	43.07										44.28	0.13	0.18
WGAJ0900.2–2817	0.894	62.3	44.20										45.42		
WGAJ0908.2+5031	0.917	105.4	43.22										44.43		
WGAJ0931.9+5533	0.266			2.4	41.96	58.5	43.08	11.1	42.33			43.25	44.43	0	
WGAJ1006.1+3236	1.020	62.4	43.98										45.19	0	
WGAJ1222.6+2934	0.787	71.1	43.92	12.3	42.90	16.8	42.62	33.6	42.89			44.02	44.94	0	
WGAJ1225.5+0715	1.120	94.8	43.39	12.3	42.48							43.91	44.42	0	
WGAJ1332.7+4722	0.668	41.4	43.51	4.2	42.35	40.2	43.10	12.0	42.57			43.57	44.65	0	
WGAJ1353.2–4720	0.550	92.9	43.79	9.7	42.56	38.1	42.93	63.9	43.12			43.97	44.76	0	
WGAJ1404.2+3413	0.937	69.2	44.74										45.95	0	
WGAJ1420.6+0650	0.236			33.2	41.69	< 5.7	<41.33	11.3	41.63	43.7	42.16	42.80	43.02	0.33	0.14
WGAJ1423.3+4830	0.569	805.6	43.77	36.3	42.47	< 21.2	<42.37	98.8	42.95			43.82	44.98	0	
WGAJ1427.9+3247	0.568			7.0	43.11	47.8	43.51	94.4	43.75			44.56	44.91	0.07	0.33
WGAJ1626.6+5809	0.748	33.2	44.44	< 1.0	<42.65	74.9	44.24	28.0	43.82			<44.53	45.65	0	
WGAJ1648.4+4104	0.851	44.8	43.78	9.7	42.98	108.1	43.74	110.2	43.75			44.53	45.01	0	
WGAJ1722.3+3103	0.305			111.9	41.75	33.0	41.92	20.7	41.72	432.2	43.07	42.87	43.80	0.32	0.51
WGAJ2056.4–5819	1.139	49.1	44.61										45.68		
WGAJ2201.6–5646	0.410	120.6	43.21			41.8	42.47	19.1	42.10	565.2	43.40	42.88	44.27	0	
WGAJ2239.7–0631	0.264			9.5	41.30	14.2	41.65	24.5	41.87	159.0	42.67	42.71	43.44	0.14	0.11
WGAJ2347.6+0852	0.292			4.6	42.03	43.3	42.98	51.1	43.06	281.0	43.22	43.78	44.19	0	
PKS 2058–425 <sup>a</sup>	0.221								13.9						
PKS 2352–342 <sup>a</sup>	0.702	38.8													

Columns: (1) object name, (2) redshift, (3) and (4) Mg II  $\lambda$ 2798, (5) and (6) [O II]  $\lambda$ 3727, (7) and (8) H $\beta$   $\lambda$ 4861, (9) and (10) [O III]  $\lambda$ 5007, (11) and (12) H $\alpha$   $\lambda$ 6563 rest frame equivalent widths and line luminosities respectively, (13) narrow line region luminosity, (14) broad line region luminosity, (15) Ca H&K break value (measured in spectra  $f_\lambda$  versus  $\lambda$ ), (16)  $1\sigma$  error on Ca H&K break value

References for emission line data: (a) Wilkes (1986)

\* lower limit since flux loss due to atmospheric differential refraction > 30 per cent

using the IRAF task *noao.onedspec.plot*. The continuum of a few objects showed the thermal shape typical for ellipticals. In these cases a local continuum was fitted to the single lines. The  $1\sigma$  uncertainties on the equivalent width and line flux values associated with the placement of the continuum are estimated to be typically  $\sim 30$  per cent and  $\sim 20$  per cent respectively. The ‘small bump’ (which spans the 2000 – 4000 Å rest frame wavelength region and is a blend of Fe II lines and Balmer continuum emission) was present in only 11 of the objects with a clearly detected [O II]  $\lambda$ 3727 emission line. In these cases the [O II] equivalent width has been determined by taking the line flux

relative to the (upper) continuum including this feature as well as to the (lower) one fitted to the entire spectrum. For these objects the typical difference between the two equivalent width values is  $\sim 20$  per cent. Since this difference is rather low compared to the measurement errors and the feature is not present in most objects, for consistency reasons the ‘uncorrected’ values are listed for these sources as well. Owing to the relatively modest S/N of our spectra we have not attempted to quantify the iron contamination of the [O III]  $\lambda$ 5007 emission line. Gaussian line profiles have been assumed for the narrow emission lines [O II]  $\lambda$ 3727 and [O III]  $\lambda$ 5007. In the case of the broad emission lines

**Table 4.** DXRBS Radio Galaxies

Name	$z$	[OII]		[OIII]		$L_{\text{NLR}}$ [erg/s]	C	$\sigma$
		$W_\lambda$ [Å]	$\log L$ [erg/s]	$W_\lambda$ [Å]	$\log L$ [erg/s]			
(1)	(2)	(3)	(4)	(5)	(6)	(7)	(8)	(9)
WGAJ0204.8+1514	0.833	49.1	42.35	85.7	42.93	43.77	0.21	0.37
WGAJ0247.9+1845	0.301	< 5.8	<40.71	< 1.8	<40.63	<41.82	0.47	0.26
WGAJ0500.0–3040	0.417	20.5	42.12	57.2	42.77	43.58	0.15	0.08
WGAJ0605.8–7556	0.458	39.8	41.21	32.9	41.18	42.33	0.03	0.24
WGAJ1120.4+5855	0.158			43.2	42.71	43.44		
WGAJ1229.4+2711	0.490	74.5	42.69	53.0	42.57	43.78	0.42	0.53
WGAJ1835.5–6539	0.554	< 4.8	<40.46	42.5	41.53	42.36	0.11	0.23
WGAJ2131.9–0556	0.085	< 9.2	<39.64	< 2.3	<39.53	<40.74	0.43	0.20
WGAJ2205.2–0004	0.827	41.1	42.15			43.59	0.36	0.75
WGAJ2303.5–5126	0.426	11.9	41.70	18.9	42.06	42.99	0.12	0.19

Columns: (1) object name, (2) redshift, (3) and (4) [O II]  $\lambda 3727$ , (5) and (6) [O III]  $\lambda 5007$  rest frame equivalent widths and line luminosities respectively, (7) narrow line region luminosity, (8) Ca H&K break value (measured in spectra  $f_\lambda$  versus  $\lambda$ ), (9)  $1\sigma$  error on Ca H&K break value

Mg II  $\lambda 2798$ , H $\beta$   $\lambda 4861$ , and H $\alpha$   $\lambda 6563$  we have not assumed a specific line profile but have integrated the line flux over the entire emission line range. This range has been determined for each object individually using the quasar composite of Francis et al. (1991) as a guide.

We have derived  $2\sigma$  upper limits on the rest frame equivalent widths and line fluxes when the lines were not detected but their position was covered by the spectrum. In the case of narrow emission lines we have determined non-detection limits only if the resolution of the spectrum was high enough to allow for a detection of an emission line with  $FWHM \leq 1000 \text{ km s}^{-1}$ . The non-detection limits have been calculated assuming a rectangular emission line. The emission line width has been assumed to be  $1000 \text{ km s}^{-1}$  for the narrow lines [O II] and [O III]. In the case of the broad lines Mg II, H $\beta$ , and H $\alpha$  we have assumed for FSRQ values  $5800 \text{ km s}^{-1}$ ,  $4000 \text{ km s}^{-1}$ , and  $4500 \text{ km s}^{-1}$  respectively, and for BL Lacs values  $4100 \text{ km s}^{-1}$ ,  $1500 \text{ km s}^{-1}$ , and  $1500 \text{ km s}^{-1}$  respectively. These correspond to the average values for the detections. We have not attempted to derive upper limits if the S/N at the position of the line was  $\lesssim 3$ .

The spectra of a number of DXRBS sources have not been observed at parallactic angle (but typically close to the meridian). We have chosen to include in our analysis line measurements based on these spectra only if the flux loss due to atmospheric differential refraction at the position of the line computed following Filippenko (1982) was less than 30 per cent.

The narrow line region (NLR) luminosity for our sources has been calculated following Rawlings & Saunders (1991) as

$$L_{\text{NLR}} = 3 \times (3 \times L_{[\text{O II}]} + 1.5 \times L_{[\text{O III}]}), \quad (1)$$

where  $L_{[\text{O II}]}$  and  $L_{[\text{O III}]}$  are the line luminosities of [O II]  $\lambda 3727$  and [O III]  $\lambda 5007$  respectively. For objects with redshifts  $z < 0.5$  for which the spectrum did not cover the position of [O II],  $L_{[\text{O II}]}$  has been calculated from the linear

correlation between the ratio  $L_{[\text{O II}]} / L_{[\text{O III}]}$  and  $\log L_{[\text{O III}]}$  found by Saunders et al. (1989). In all other cases the relation  $L_{[\text{O III}]} = 4 \times L_{[\text{O II}]}$  has been used when the spectrum covered the position of only one of the two emission lines. The broad line region (BLR) luminosity was calculated following Celotti et al. (1997) as:

$$L_{\text{BLR}} = \sum_i L_{i,obs} \frac{\langle L_{\text{BLR}}^* \rangle}{\sum_i L_{i,est}^*}, \quad (2)$$

where  $\sum_i L_{i,obs}$  is the sum of the measured luminosities of the observed broad lines, scaled by the ratio of the estimated total broad line region luminosity  $L_{\text{BLR}}^*$  to the estimated luminosities of the observed broad lines. Both estimates were taken from the results of Francis et al. (1991), and in the case of H $\alpha$   $\lambda 6563$  from Gaskell et al. (1981).

#### 4 THE LIMITATIONS OF THE CURRENT CLASSIFICATION SCHEME

We have initially classified objects in the DXRBS sample as BL Lacs and FSRQ following the scheme proposed by Marchã et al. (1996). These authors suggested to use the strength of the Ca H&K break and the equivalent width of the strongest *observed* emission line to separate classes of radio-loud AGN.

The Ca H&K break is a prominent absorption feature typically seen in the spectra of elliptical galaxies (the hosts of radio-loud AGN; e.g., Wurtz et al. 1996) and is located at  $\sim 4000 \text{ Å}$  rest frame wavelength. It is defined as  $C = (f_+ - f_-) / f_+$ , where  $f_-$  and  $f_+$  are the fluxes in the rest frame wavelength regions  $3750 - 3950 \text{ Å}$  and  $4050 - 4250 \text{ Å}$  respectively. Its value in normal non-active ellipticals is on average  $\sim 0.5$  (Dressler & Shectman 1987). In blazars the value of the Ca H&K break is assumed to be decreased by the presence of non-thermal jet emission.

An increase of the non-thermal jet continuum, however,

will also lead to a decrease of the equivalent width of any blazar emission line (assuming a roughly constant ionizing continuum and so line flux). Therefore, Marchã et al. proposed to use the Ca H&K break value – equivalent width plane to classify radio-loud AGN. In particular, they proposed to classify in this plane objects with Ca H&K break values  $C \leq 0.4$  and  $C > 0.4$  as blazars and radio galaxies respectively. This was based on their reinvestigation of the sample of Dressler & Sheckman (1987) which yielded that less than 5 per cent of non-active ellipticals had Ca H&K break values  $C \leq 0.4$ . In a previous paper (Landt et al. 2002) we have shown that the transition in Ca H&K break value from blazars to radio galaxies is rather continuous, since this feature is decreased by the amplified jet due to a change in viewing angle. However, our studies showed that low-luminosity radio-loud AGN become increasingly radio core-dominated around  $C \sim 0.35$ , a value similar to the one proposed by Marchã et al. to separate blazars from radio galaxies but with a more physical meaning.

The blazar class itself was divided by Marchã et al. using a diagonal line in the Ca H&K break value – equivalent width plane (see Fig. 1). This line represented the simulated increase in emission line equivalent width with decreasing non-thermal jet continuum (i.e., with increasing Ca H&K break value) for the well-known BL Lac object 3C 371. These authors assumed that 3C 371 was representative for the BL Lac class and argued that all objects with weaker emission lines (left of the diagonal line) should be classified as BL Lacs, whereas those with stronger emission lines (right of the diagonal line) should be classified as quasars.

Using the Ca H&K break value – equivalent width plane to classify radio-loud AGN the way it was suggested by Marchã et al. is problematic for the following reasons:

(i) The diagonal line that separates BL Lacs and FSRQ is not only arbitrary, but might contribute to the observed rareness of high-redshift BL Lacs in present samples (see below).

(ii) If the Ca H&K break value – equivalent width plane is to be used to separate both blazars and radio galaxies it has to be applied to narrow emission lines (and not to the strongest *observed* emission line), since only these are common to both.

(iii) In any case, the rest frame equivalent width of broad emission lines is not necessarily expected to decrease with decreasing Ca H&K break value, if this is indeed a suitable viewing angle indicator (Landt et al. 2002).

In the following subsections we expand on these points.

#### 4.1 The Redshift Effect

In Fig. 1 we plot the Ca H&K break value versus the rest frame equivalent width of the strongest observed emission line for the objects in our sample. We have measured Ca H&K break values in spectra plotted as  $f_\lambda$  versus  $\lambda$  and have derived their  $1\sigma$  errors based on the S/N blueward and redward of the feature (Tables 1 and 2). We consider the Ca H&K break to have reached its minimum value of zero when the flux blueward of this feature is equal to or larger

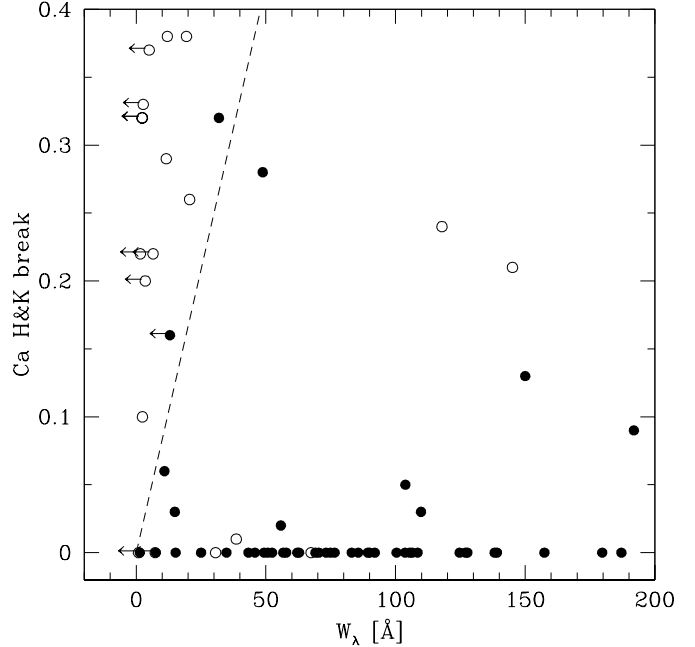


**Figure 1.** The Ca H&K break value versus the rest frame equivalent width of the strongest observed emission line for DXRBS BL Lacs and FSRQ. Open and filled circles indicate objects with redshifts  $z < 0.4$  and  $z \geq 0.4$  respectively. Arrows indicate upper limits. WGAJ0322.1-5205, WGAJ0539.0-3427, WGAJ0546.6-6415, and WGAJ0631.9-5404 are off the plot to the right. The dashed line represents the division between BL Lacs and FSRQ proposed by Marchã et al. (1996).

than the one redward. The Ca H&K break is observable in the optical spectrum up to a redshift of  $z \sim 1.2$ . Therefore, we have included in Fig. 1 all BL Lacs and FSRQ from our sample with redshifts below this value, with the exception of 16 objects (the spectrum of 10 objects does not cover the Ca H&K break location, and for 6 objects the Ca H&K break is located at the position of strong telluric absorption or is sampled with poor S/N). Due to the redshift restriction the strongest emission lines observed in these objects are Mg II  $\lambda 2798$ , [O II]  $\lambda 3727$ , H $\beta$   $\lambda 4861$ , [O III]  $\lambda 5007$ , and H $\alpha$   $\lambda 6563$ .

We first notice that the large majority (44/70 or 62.9 per cent) of the sources plotted in Fig. 1 have a Ca H&K break diluted to its minimum value of zero. This is not surprising, since efficiently selected blazar samples are expected to include mainly strongly beamed sources, i.e., sources with Ca H&K break values of  $C = 0$ . At  $C = 0$ , however, the diagonal line suggested by Marchã et al. to separate blazars (dashed line in Fig. 1) does not allow any *emission* lines for BL Lacs. Moreover, most sources with  $C = 0$  are not expected to have detectable *absorption* lines, since these will be diluted by the beamed jet emission. It then follows that for efficiently selected blazar samples the current classification scheme defines BL Lacs as those sources without *any* feature.

This has strong implications for the redshift distribu-



tion of current blazar surveys, which also include weakly beamed sources (i.e., sources with  $C > 0$ ). As discussed above, only weakly beamed BL Lacs will have a redshift determination, while no restriction applies for FSRQ. In flux-limited samples, however, strongly beamed sources will have higher powers and so will be detected at higher redshifts. Indeed, in Fig. 1, 48 objects have a redshift  $z \geq 0.4$  (filled circles) and of these 38 objects (or 79.2 per cent) have a Ca H&K break value  $C = 0$ , i.e., are highly beamed. As a consequence, the Marchã et al. dividing line biases the BL Lac redshift distribution towards lower values. A similar bias against high-redshift BL Lacs was not introduced by the ‘original’ classification criteria of the EMSS and 1 Jy surveys. These allowed emission features (with  $W_\lambda < 5 \text{ \AA}$ ) for sources with  $C = 0$ .

In this context we would like to point out that, unlike DXRBS, other recent blazar surveys did not strictly follow the Marchã et al. classification scheme. For example, RGB (Laurent-Muehleisen et al. 1999), REX (Caccianiga et al. 1999) and CLASS (Caccianiga et al. 2002) classified as BL Lacs all sources with  $C < 0.25$  and  $W_\lambda < 5 \text{ \AA}$ , i.e., they allowed emission lines at  $C = 0$ , contrary to what the Marchã et al. dividing line suggests. Therefore a severe redshift bias due to classification is not expected in these surveys.

#### 4.2 The Ca H&K Break Value – Equivalent Width Plane

We now want to investigate if it is in general physically justified to separate blazars in the Ca H&K break value – equivalent width plane.

Recently, we have shown that the Ca H&K break value of BL Lacs and low-luminosity radio galaxies decreases with viewing angle (Landt et al. 2002). This, however, means that only the equivalent widths of narrow emission lines, believed to be isotropic, are expected to decrease with Ca H&K break value. The broad emission lines, on the other hand, will be obscured by the putative circumnuclear dusty torus at relatively large viewing angles, and will come progressively into our line of sight as the viewing angle, and therefore the Ca H&K break, decreases. Simultaneously we also expect the continuum flux to increase (owing to the beamed jet component). This combination of emission line and continuum flux increase renders the resulting equivalent width and its dependence on the Ca H&K break value difficult to quantify and the possibility remains that the equivalent widths of broad emission lines *increase* with Ca H&K break value. Moreover, if the Ca H&K break value – equivalent width plane is to be used to separate also radio galaxies and blazars (as was suggested by Marchã et al.) it is obvious that it has to be applied to narrow emission lines only. Thus the question that we want to answer becomes: Is it physically justified to separate blazars in the Ca H&K break value – equivalent width plane using their *narrow* emission lines? In the following we consider the strongest of the narrow emission lines typically seen in radio-loud AGN, namely [O II]  $\lambda 3727$  and [O III]  $\lambda 5007$ .

For our studies we have first simulated the decrease in equivalent width with decreasing Ca H&K break value.

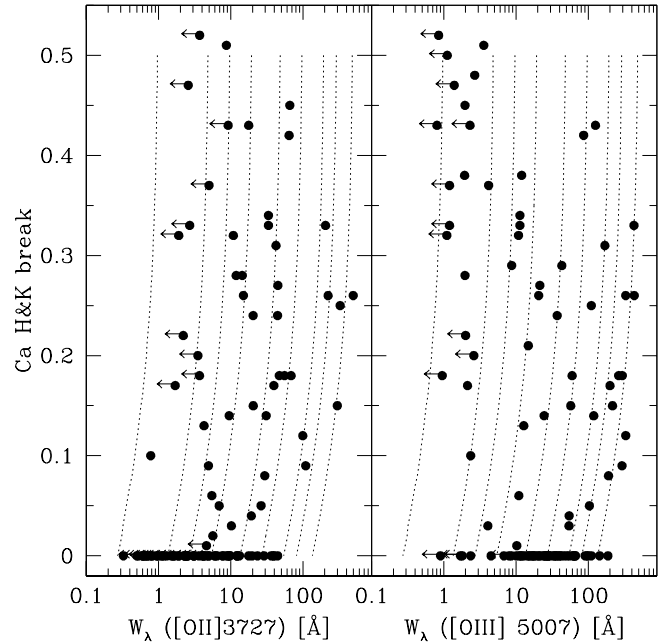


**Figure 2.** The Ca H&K break value versus the [O II]  $\lambda 3727$  (left panel) and [O III]  $\lambda 5007$  rest frame equivalent width (right panel) for DXRBS and 2 Jy objects. Arrows indicate upper limits. Dotted lines represent the simulated decrease in rest frame equivalent width with increasing non-thermal continuum contribution (see text for details) for a starting value (at  $C = 0.5$ ) of  $W_\lambda = 1, 5, 10, 20, 50, 100, 200, 300,$  and  $500 \text{ \AA}$  (from left to right).

We have assumed at  $C = 0.5$  starting equivalent width values  $W_\lambda = 1, 5, 10, 20, 50, 100, 200, 300,$  and  $500 \text{ \AA}$ , and have increased the non-thermal jet emission  $f_{\text{jet}}$  relative to a constant host galaxy flux  $f_{\text{gal}}$ . The corresponding Ca H&K break value  $C$  was calculated using the relation  $\log f_{\text{jet}}/f_{\text{gal}} = -3.74 \times C + 0.43$ , which results from the simulations presented in Landt et al. (2002) for a jet of optical spectral index  $\alpha_\nu = 1$  (see their Fig. 2). The resulting correlations between Ca H&K break value and equivalent width are represented by the dotted lines in Fig. 2. We note that, contrary to the results of Marchã et al., the above relation between Ca H&K break value and jet emission gives a non-linear dependence between the Ca H&K break and equivalent width values. For a change in the optical spectral index of the jet of  $\pm 1$  the predicted equivalent widths at  $C = 0$  change by a factor of  $\sim 2$ .

Our simulations show that the equivalent width range of objects with high Ca H&K break values determines the maximum equivalent width range of objects with low Ca H&K break values. Note that it is the maximum range, since an increasing jet emission can further decrease the equivalent width, although the Ca H&K break value has reached its minimum value of zero. This means that the equivalent width range of blazars depends on the (intrinsic) equivalent width range of their parent radio galaxy populations. A separation of blazars into subclasses using, e.g., one of the simulated dashed lines, would then be physically justified only

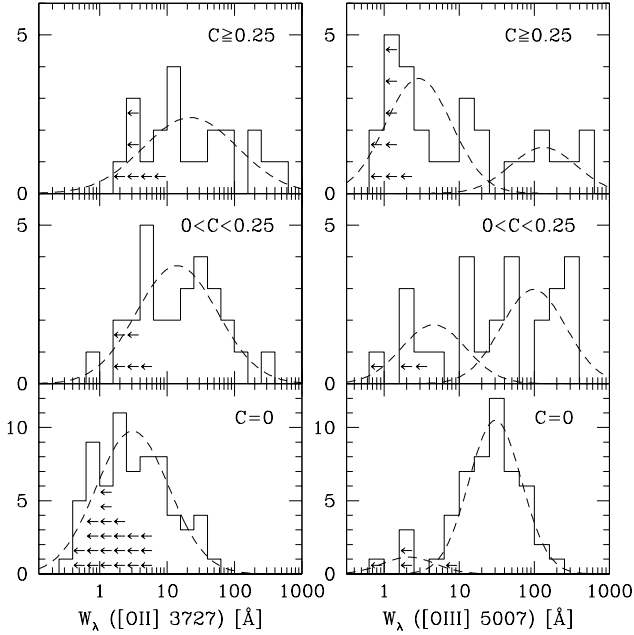


**Figure 3.** The [O II]  $\lambda 3727$  and [O III]  $\lambda 5007$  rest frame equivalent width distributions for objects with  $C = 0$ ,  $0 < C < 0.25$ , and  $C \geq 0.25$  from the DXRBS and 2 Jy survey. Arrows indicate upper limits. The dashed curves represent the best-fit Gaussian models.

if there also existed two populations of radio galaxies with significantly different [O II] and/or [O III] equivalent width distributions. In other words, we need to observe a bimodal [O II] and/or [O III] line luminosity distribution intrinsic to the entire class of radio-loud AGN, which is expected to manifest itself as a bimodal equivalent width distribution at any given orientation. Note that equivalent width, although orientation dependent in radio-loud AGN, is independent of redshift<sup>1</sup> and so more appropriate than line luminosity to quantify in a meaningful way such a bimodality.

In order to investigate the existence of a bimodality intrinsic to the class of radio-loud AGN we need a large number of sources that span a wide range of equivalent widths and Ca H&K break values. Therefore, we have added to our sample SSRQ and radio galaxies from the DXRBS (see Sections 2.3 and 2.4). Given its radio spectral index cut ( $\alpha_r \leq 0.7$ ), however, DXRBS selects against most radio galaxies. We have then included also the sample of radio galaxies and quasars from the 2 Jy survey presented by Tadhunter et al. (1993) and Morganti et al. (1997). We believe that the use of objects from radio surveys with different flux limits is warranted and should not introduce any bias since line flux was not part of the selection criteria.

In Fig. 2 we plot the Ca H&K break value versus the rest frame equivalent width of [O II]  $\lambda 3727$  (left panel) and [O III]  $\lambda 5007$  (right panel) for radio-loud AGN from the

DXRBS and 2 Jy survey. In the left (right) panel of Fig. 2 we have included 77 (61) and 39 (45) sources from the DXRBS and 2 Jy sample respectively. We note that we have excluded from our studies sources with errors on the Ca H&K break value  $> 0.2$ . In Fig. 3 we show the equivalent width distributions for these objects, binned into three groups of Ca H&K break values  $C = 0$ ,  $0 < C < 0.25$  and  $C \geq 0.25$ . These groups comprise 67, 28 and 21 objects respectively in the case of [O II], and 52, 26 and 28 objects respectively in the case of [O III].

In order to quantify a possible bimodality in these distributions we have used the KMM algorithm (Ashman et al. 1994). The KMM algorithm computes for a given univariate dataset the confidence level at which the single Gaussian model can be rejected in favor of a two Gaussian model. We have fitted homoscedastic groups (i.e., groups with similar covariances), and only if the resulting confidence level was below 95 per cent have we also considered the heteroscedastic case. For the distributions in Fig. 3 we get a high confidence level for the rejection of the single Gaussian model in the case of [O III] for objects with  $C \geq 0.25$  ( $P = 99.0$  per cent) and  $C = 0$  ( $P = 98.5$  per cent), and a lower significance for objects with  $0 < C < 0.25$  ( $P = 90.2$  per cent). For [O II] a single Gaussian model is always the best fit. We have overlaid the resulting best-fit Gaussians as dashed lines in Fig. 3. We note that the KMM algorithm does not consider censoring in the data which is present for both [O II] and [O III] in all Ca H&K break value bins. Since these limits are *all* at the lower end of the distributions, the significance of the bimodality would increase in all cases if these limits were taken into account. Therefore, a bimodality cannot be excluded also in the case of [O II].

The single Gaussian models for the [O II] equivalent width distributions give mean values of about 22, 14, and 3 Å for objects with  $C \geq 0.25$ ,  $0 < C < 0.25$ , and  $C = 0$  respectively. This observed decrease in equivalent width is well reproduced by our simulations that give at  $C = 0$  a value of  $\sim 5$  Å if we assume a starting value of  $\sim 20$  Å at  $C = 0.5$ . This further confirms the use of the Ca H&K break as a statistical beaming indicator. In the case of [O III] we get mean values for the two best-fit Gaussians of  $\sim 3$  and 135 Å for objects with  $C \geq 0.25$ , and  $\sim 5$  and 100 Å for objects with  $0 < C < 0.25$ . For starting values of  $\sim 5$  and 140 Å our simulations predict values of  $\sim 1.5$  and 40 Å at  $C = 0$ . This is similar to the means of  $\sim 2$  and 30 Å observed for objects with  $C = 0$ .

Therefore, although the observed bimodality in the case of sources with  $0 < C < 0.25$  is only marginally significant (but see above), the [O III] bimodality for radio-loud AGN appears to have physical reality. Relativistic beaming simulations give values in good agreement with the observed decrease of the mean of the two modes with Ca H&K break. Assuming no bimodality for objects with  $C \geq 0.25$  would result in a best-fit single Gaussian model with a mean of  $\sim 10$  Å, which is *smaller* than the mean of  $\sim 20$  Å that results for a best-fit single Gaussian model for objects with  $C = 0$ . In other words, only a bimodality for objects with  $C \geq 0.25$  can account for the values observed in blazars within the beaming scenario. We note, however, that objects

<sup>1</sup> This is not strictly true for sources with continua dominated by the host galaxy, i.e., for sources with  $C \geq 0.25$  (see § 6.3).

with  $C = 0$  and very small [O III] equivalent widths seem to be underrepresented in our sample. The missing sources are most likely the featureless BL Lacs with no available redshift. In the DXRBS there are 13 such objects (5 of which have been observed by us) that have been excluded from our analysis. Tadhunter et al. (1993) failed to identify recognizable features for 11 sources out of their complete sample of 87 2 Jy sources.

## 5 A PHYSICAL CLASSIFICATION SCHEME

We want now to investigate the most appropriate way to separate all radio-loud AGN (blazars and radio galaxies) into sources with *intrinsically* weak and strong [O III] emission lines, which we dub weak- and strong-lined radio-loud AGN respectively. In a future paper (Landt et al., in prep.) we will investigate in detail the possible underlying physical differences between the two classes.

### 5.1 The [O III] – [O II] Equivalent Width Plane

One option to split a sample of radio-loud AGN into weak- and strong-lined sources would be to use as a dividing line one of the simulated lines in the Ca H&K break value – [O III] equivalent width plot. Then, one could think of using simply the simulated line corresponding at  $C = 0.5$  to the value of the intersection point of the two best-fit Gaussians for objects with  $C \geq 0.25$ . However, a large fraction (52/106 or 49 per cent) of the sources included in Fig. 2 (right panel) have  $C = 0$ . For these objects the dividing value at  $C = 0$  resulting from our simulations could be problematic, since, as mentioned earlier, the equivalent width will continue to decrease with increasing jet emission, although the Ca H&K break has reached its minimum value. In other words, at  $C = 0$  extremely beamed strong-lined AGN can cross the dividing line and invade the region of weak-lined AGN, or, put differently, at  $C = 0$  it becomes impossible to distinguish between ‘intrinsically’ weak-lined sources and those appearing weak because they are strongly beamed. This means that the Ca H&K break value – equivalent width plane simply does not offer the dynamic range necessary for a meaningful separation of *all* radio-loud AGN into weak- and strong-lined sources.

Such a separation, however, has to be based in any case on the [O III] equivalent width (the [O III] line luminosity is not an option, since it depends strongly on redshift), but this requires a method to disentangle orientation effects if radio galaxies and blazars are included. We suggest that this is possible using an [O III]  $\lambda 5007$  – [O II]  $\lambda 3727$  equivalent width plot. Since the equivalent widths of both these emission lines are expected to decrease with viewing angle, in such a plot objects viewed at larger and smaller angles are expected to be concentrated at higher and lower [O II] and [O III] equivalent width values respectively, and so to populate distinct regions of the plane.

In Fig. 4 we have plotted the [O III]  $\lambda 5007$  versus the [O II]  $\lambda 3727$  rest frame equivalent widths for objects from the DXRBS and 2 Jy survey (118 objects). In order to increase

the number statistics we have added objects with errors on their Ca H&K break values  $> 0.2$  (17 sources; mean error 0.3), and objects with no available Ca H&K break measurement (8 sources). We have plotted objects with Ca H&K break values  $C \geq 0.25$ ,  $0 < C < 0.25$  and  $C = 0$  as stars (32 objects), open squares (30 objects), and filled circles (48 objects) respectively. In cases where a Ca H&K break measurement was not available, we have assumed that objects are viewed at relatively small angles if broad emission lines were present in their optical spectra (6 objects, grouped with sources with  $C = 0$  and plotted as filled circles), and that they are viewed at relatively large angles if only narrow lines had been observed (2 objects, grouped with sources with  $C \geq 0.25$  and plotted as stars).

Fig. 4 shows that, as anticipated, sources with relatively high and low Ca H&K break values, i.e., weakly and strongly beamed sources respectively, separate in this plane. Also, as argued in Section 4, the majority of our blazars appear to be beamed radio galaxies with strong [O III] emission lines, since it is mostly this type of radio galaxies that have [O III] and [O II] equivalent widths higher than those of blazars. (Note that these quantities are expected to decrease with viewing angle only if radio galaxies and blazars are part of the same population.)

We now want to assess the most appropriate separation scheme for weak- and strong-lined radio-loud AGN in the [O III] – [O II] equivalent width plane applicable to *both* radio galaxies and blazars. A striking feature of Fig. 4 is the clear-cut upper envelope that extends from sources with high Ca H&K break values to those with low Ca H&K break values, i.e., from radio galaxies to blazars, for which we get roughly a slope of  $\sim 0.4$ . We assume that this represents the general relation between the [O III] and [O II] equivalent widths of radio-loud AGN as the viewing angle changes, and have attempted to reproduce it. We have assumed two components for the continuum, jet and host galaxy, and let the jet emission increase relatively to the host galaxy (jet/galaxy ratio defined at  $5500 \text{ \AA}$ ) as the angle with respect to the line of sight decreases. We have assumed starting [O III] equivalent width values  $W_{[\text{O III}]} = 200, 50$  and  $20 \text{ \AA}$  and a constant line luminosity ratio  $L_{[\text{O II}]} / L_{[\text{O III}]} = 0.3$  (the mean value for the 84 objects in our sample with both a detected [O II] and [O III] emission line). For the jet we have assumed a power-law spectrum with spectral index  $\alpha_\nu = 1$ . Our results are shown in Fig. 4 as the rightmost set of dashed and dotted lines, which indicate loci of objects with Ca H&K break values  $C > 0$  and  $C = 0$  respectively. For a change in the optical spectral index of the jet of  $\pm 1$  the predicted equivalent widths for sources with  $C = 0$  change by a factor of  $\sim 2$ .

Our simulations reproduce well the equivalent width decrease for objects with  $C > 0$  as well as the position at which sources start to have a Ca H&K break value of zero. However, the predicted relation between the [O II] and [O III] equivalent widths in the regime of sources with  $C = 0$  is steeper than the envelope to the data. In our simulations the Ca H&K break is diluted to its minimum value of zero when the jet emission dominates at all optical wavelengths. As the jet emission increases further both the [O II] and

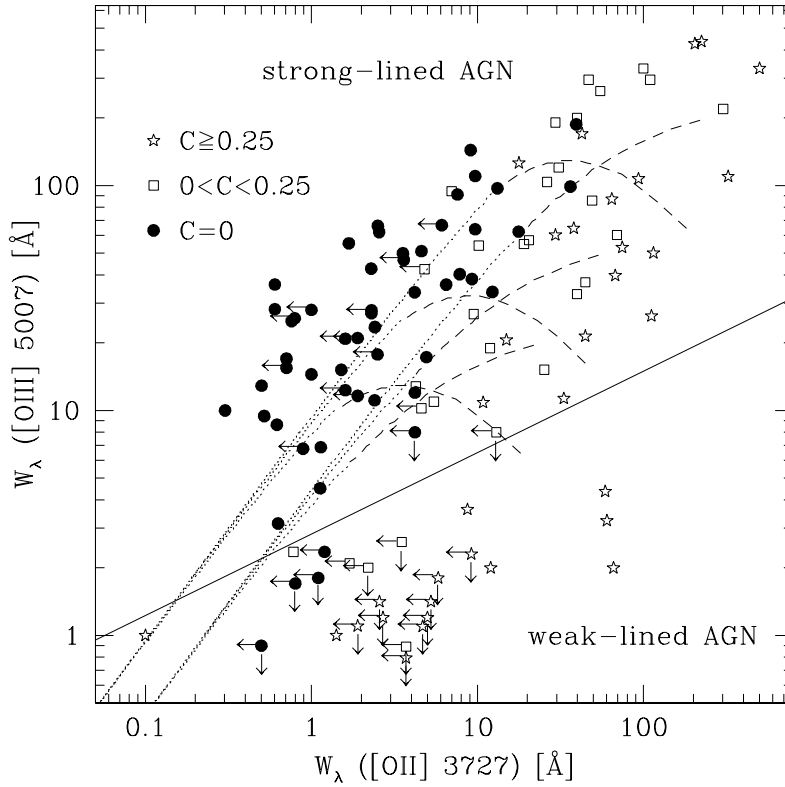


**Figure 4.** The rest frame equivalent widths of [O III]  $\lambda 5007$  versus [O II]  $\lambda 3727$  for objects from the DXRBS and 2 Jy survey. Filled circles, open squares and stars represent sources with Ca H&K break values  $C = 0$ ,  $0 < C < 0.25$  and  $C \geq 0.25$  respectively. Arrows indicate upper limits. The dashed and dotted lines represent simulated loci of objects with  $C > 0$  and  $C = 0$  respectively. The solid line separates weak- (below the line) and strong-lined radio-loud AGN (above the line) as defined in our studies (Section 5.3). See text for details.

[O III] equivalent widths decrease in a similar way, resulting in a correlation between the two with a slope of one. This is shown by the dotted lines in Fig. 4 which converge irrespective of the starting [O III] equivalent width values. But the envelope assumed to represent the general relation between the [O III] and [O II] equivalent widths of radio-loud AGN has a slope flatter than one. This means that with decreasing viewing angle either the line luminosity ratio  $L_{[\text{OII}]} / L_{[\text{OIII}]}$  decreases or the continuum at the position of [O II] increases more than the one at the position of [O III].

The first possibility, namely that the line luminosity ratio  $L_{[\text{OII}]} / L_{[\text{OIII}]}$  decreases with viewing angle, could be the case if, e.g., the [O III] emission was anisotropic (Hes et al. 1996). Indeed, for the objects in our sample with a detection of at least one of the two emission lines and errors on the Ca H&K break value  $< 0.2$  we find a strong ( $P > 99.9$  per cent) correlation between  $L_{[\text{OII}]} / L_{[\text{OIII}]}$  and Ca H&K break value, albeit with a large scatter. We have used here and in the following the ASURV analysis package (Isobe et al. 1986) whenever censoring was present in our data.

In order to test if an increase of the [O III] line flux with decreasing viewing angle can in fact account for the distribution of the points in Fig. 4 we have repeated the simulations. We have now assumed starting [O II] (and not [O III] as before) equivalent widths  $W_{[\text{O II}]} = 200, 50$  and  $20 \text{ \AA}$  and increased the [O III] line flux in dependence of the Ca H&K break value using the above correlation between  $L_{[\text{OII}]} / L_{[\text{OIII}]}$  and Ca H&K break value. The results are shown in Fig. 4 as the leftmost set of dashed and dotted lines, indicating loci of objects with Ca H&K break values  $C > 0$  and  $C = 0$  respectively. This new set of simulations seems to reproduce the equivalent width decrease for objects with  $C > 0$  worse than the earlier one. Moreover, it still cannot reproduce the upper envelope to the data. This is because the increase in jet emission ‘catches up’ with the [O III] line flux increase, causing the [O II] and [O III] equivalent widths to decrease in a similar way as soon as the Ca H&K break is diluted to its minimum value.

The second possibility, namely that the continuum at the position of [O II] increases with decreasing viewing angle

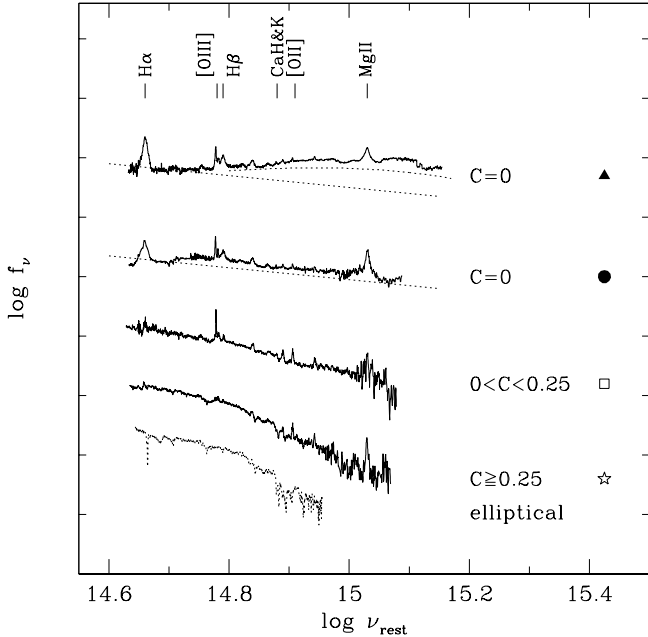


**Figure 5.** Composite spectra for objects from the DXRBS and 2 Jy survey grouped according to their Ca H&K break value. Also shown is the spectrum of an elliptical galaxy. A power law continuum with slope  $\alpha_\nu = 1$  and a Balmer continuum are underlaid as dotted lines to the composites for objects with Ca H&K break value  $C = 0$ . Objects included in the composites are plotted in Fig. 6 with symbols shown on the right side. Objects with  $C = 0$  are separated into sources with optical spectral slopes between the rest frame frequencies of [O II] and [O III] below (top, triangle) and above (bottom, circle)  $\alpha_{\text{OIII}}^{\text{OII}} = 1$ .

more than the one at the position of [O III], already applies to sources with  $C > 0$ . The difference in spectral shape between the two continuum components, jet and host galaxy, is such that in these sources the total continuum increases mainly at shorter wavelengths. For sources with  $C = 0$ , however, where the jet emission dominates, this is only possible if we assume a third component that starts to appear at UV frequencies at the smallest viewing angles.

The accretion disc believed to surround the central black holes of all AGN, although neglected in our simulations, cannot be this additional component. Assuming a constant emission line ratio, a linear relation with a slope less than one between the logarithmic [O II] and [O III] equivalent width values implies that the continuum spectral slope between the rest frame frequencies of [O II] and [O III] ( $\alpha_{\text{OIII}}^{\text{OII}}$ ) is not constant but decreases with equivalent width. Then, for example, for a constant emission line ratio of  $L_{[\text{OII}]} / L_{[\text{OIII}]} = 0.3$  a slope of  $\sim 0.4$  for the linear relation between the logarithmic [O II] and [O III] equivalent width values implies extremely ‘blue’ optical spectral slopes for objects with the smallest equivalent widths (e.g.,  $\alpha_{\text{OIII}}^{\text{OII}} \sim -4$  if  $W_{[\text{O II}]} \sim 3$ ). This means that the additional component needs either to have  $\alpha_{\text{OIII}}^{\text{OII}}$  much flatter than one, i.e., much flatter than the spectral slope assumed for the jet, or to cover only the lo-

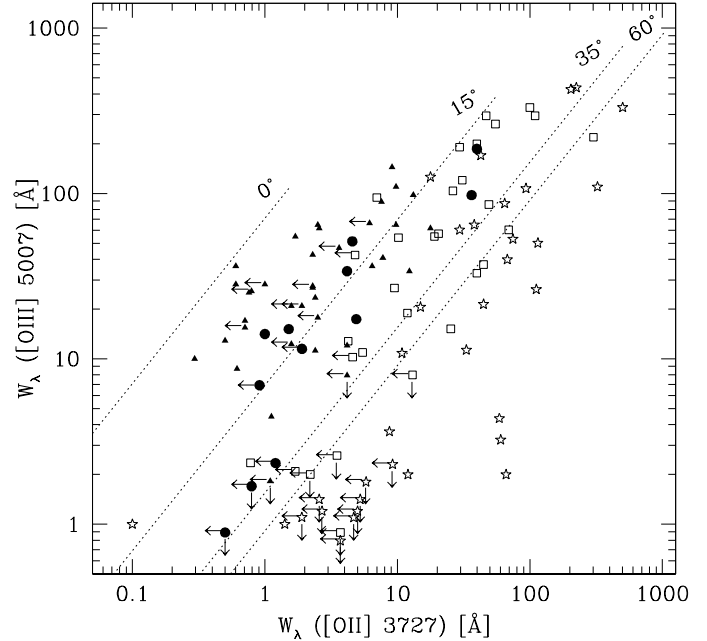


**Figure 6.** The rest frame equivalent widths of [O III]  $\lambda 5007$  versus [O II]  $\lambda 3727$  for objects from the DXRBS and 2 Jy survey. Symbols are as in Fig. 5. Arrows indicate upper limits. Dotted lines represent loci of constant viewing angle as labeled (see text for details).

cation of [O II]. The accretion disc spectrum, however, is believed to extend over a large range of frequencies covering the locations of both [O III] and [O II] and is in general approximated in the optical/near-UV regime by a power law of the form  $S_\nu \propto \nu^{1/3}$  (e.g., Czerny & Elvis 1987; Koratkar & Blaes 1999). Furthermore, D’Elia et al. (2003) have shown that the thermal (disc) component in DXRBS FSRQ makes up, on average, only  $\sim 15$  per cent of the optical/UV emission in these sources.

In the following we want to assess if an additional component with the required properties is indeed present in the spectra of radio-loud AGN viewed at the smallest angles.

## 5.2 The Continuum Emission of Radio-Loud AGN

For our sources from the DXRBS and 2 Jy survey we have built composite spectra for objects with Ca H&K break values  $C \geq 0.25$ ,  $0 < C < 0.25$  and  $C = 0$ , the latter separated also into sources with  $\alpha_{\text{OIII}}^{\text{OII}} \geq 1$  and  $< 1$  (calculated from the ratios between their [O II] and [O III] continuum luminosities). Before combining them we have shifted the spectra to their rest frame wavelength, normalized at  $5500 \text{ \AA}$  and trimmed off noisy edges. We have merged the spectra building an average with the IRAF task *noao.onedspec.scombine*. The resulting four composites are displayed in Fig. 5. From top to bottom these contain 37, 12, 28 and 34 objects.

Our composites show that as expected the continuum of radio-loud AGN flattens with decreasing Ca H&K break value. The simplest interpretation seems to be indeed that

the observed flattening results from different components dominating the continuum emission at different orientations. A comparison between the composite for objects with  $C \geq 0.25$  and the spectrum of an elliptical galaxy (dotted spectrum in Fig. 5) confirms that the galaxy component dominates at large viewing angles. As the viewing angle decreases and relativistic beaming enhances the jet emission, the continuum flattens (composite for objects with  $0 < C < 0.25$ ) until the jet emission dominates (lower composite for objects with  $C = 0$  to which a power-law spectrum with slope  $\alpha_\nu = 1$  is overlaid as dotted line). Finally, a group of sources with  $C = 0$  whose continuum emission at UV frequencies is dominated by a third component is also present (upper composite for objects with  $C = 0$ ). According to our earlier considerations these sources are expected to be viewed at the smallest angles.

The additional component is most likely the ultraviolet excess often observed in AGN and interpreted as Balmer continuum/Fe II emission (e.g., Malkan & Sargent 1982). Following Wills et al. (1985) we have then calculated the Balmer continuum for a temperature of 15,000 K and have overlaid the resulting spectrum as the dotted curve to the upper composite for objects with  $C = 0$ . A remarkable agreement is evident. But is it feasible to assume that the Balmer continuum emission starts to dominate at the smallest viewing angles? Observations indicate that the Balmer continuum is located within the BLR (Maoz et al. 1993). Therefore, as the broad emission lines themselves we expect the Balmer continuum to be obscured by the putative circumnuclear dusty torus at large viewing angles and to come into our line of sight only if the AGN is oriented at relatively small viewing angles.

To explain the distribution of points in Fig. 4 we have then repeated our simulations assuming now three components for the continuum emission of radio-loud AGN, namely host galaxy, jet and Balmer continuum, and increased the flux of the latter two with decreasing viewing angle. We have simulated the change in orientation by increasing the jet flux relative to the host galaxy emission (jet/galaxy ratio defined at 5500 Å) and calculated from this viewing angles using our results presented in Landt et al. (2002). In particular we have derived a relation between jet/galaxy ratio and viewing angle using from these studies the linear relation between jet/galaxy ratio and Ca H&K break value for a jet with spectral slope  $\alpha_\nu = 1$ , and the linear relation between Ca H&K break value and viewing angle for a jet with Lorentz factor  $\Gamma = 3$ . We have assumed that these relations are valid for all radio-loud AGN. The flux increase of the Balmer continuum with decreasing viewing angle has been adjusted interactively to give a slope of  $\sim 0.4$  for the correlation between the logarithmic [O III] and [O II] equivalent widths. The resulting loci of constant viewing angle are shown as dotted lines in Fig. 6. These have a slope of one, since we have assumed for simplicity a constant line luminosity ratio  $L_{[\text{O III}]} / L_{[\text{O II}]}$  which does not change with viewing angle, but the envelope of these lines follows the slope of the envelope to the data points.

These revised simulations predict that the continuum flux at the position of [O II] is dominated by emission

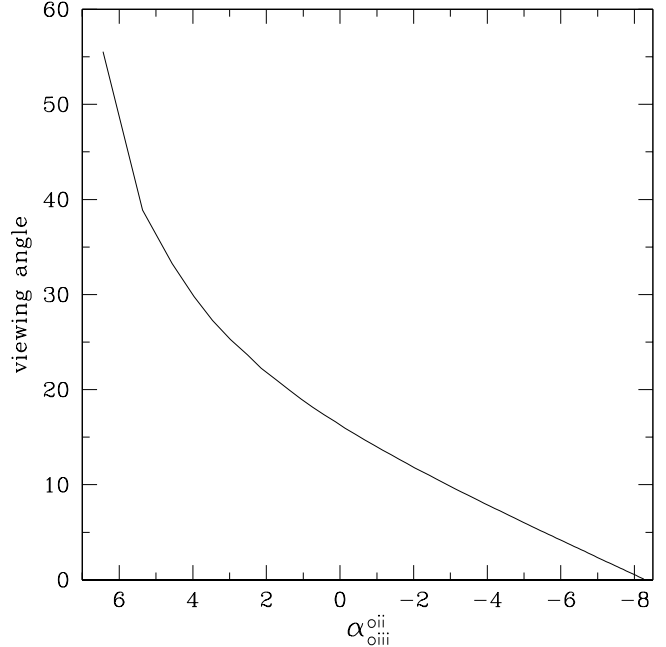


**Figure 7.** The relation viewing angle versus continuum optical spectral slope (between the rest frame frequencies of [O II]  $\lambda 3727$  and [O III]  $\lambda 5007$ ) as obtained from our simulations.

from the host galaxy, jet, and Balmer continuum for objects viewed at angles  $\phi \gtrsim 35^\circ$ ,  $15^\circ \lesssim \phi \lesssim 35^\circ$  and  $\phi \lesssim 15^\circ$  respectively. In Fig. 6 we have also plotted objects included in the four composites with different symbols. From this we see in particular that objects with  $C = 0$  included in the upper and lower composites (filled triangles and circles respectively) cluster around the predicted values (and so are indeed sources viewed at smaller and larger angles respectively). Therefore, the continuum of radio-loud AGN appears to change with viewing angle mainly at the position of [O II] rendering the optical spectral slope  $\alpha_{\text{oiiii}}^{\text{oi}}$  a suitable orientation indicator. Fig. 7 shows its relation to viewing angle as obtained from our simulations. Note that  $\alpha_{\text{oiiii}}^{\text{oi}}$  has more extreme values than those of the ‘usual’ optical continuum spectral slopes since it is measured over a much narrower frequency range. The parameter  $\alpha_{\text{oiiii}}^{\text{oi}}$  is directly related to the Ca H&K break value, the [O II] and [O III] emission lines being located blue- and redward of this feature respectively, but it offers a much higher dynamical range.

In this context, we note that it has been argued that some radio-loud AGN with weak emission lines might not possess significant broad line regions and/or nuclear absorbing structures (e.g., Chiaberge et al. 1999, 2002). For these sources the relation between the parameter  $\alpha_{\text{oiiii}}^{\text{oi}}$  and viewing angle shown in Fig. 7 will not be valid. Moreover, in their case  $\alpha_{\text{oiiii}}^{\text{oi}}$  will not be a ‘better’ orientation indicator than the Ca H&K break value, since for  $C = 0$  its value will be simply the optical spectral index of the jet. Similarly, these sources are expected to cluster around a line with slope of one (and not of slope  $\sim 0.4$ ) in the [O III] – [O II] equivalent width plane, once  $C = 0$  is reached.

### 5.3 Weak- and Strong-Lined Radio-Loud AGN

We now want to use the [O III] – [O II] equivalent width plane to separate our sources into weak- and strong-lined radio-loud AGN. For the objects plotted in Fig. 4 we get [O III] and [O II] equivalent width distributions similar to the ones shown in Fig. 3. The intersection point of the two best-fit Gaussians for objects with  $C \geq 0.25$  is  $W_{[\text{O III}]} \sim 10 \text{ \AA}$ . We then define the line dividing weak- and strong-lined radio-loud AGN in this plane to have a slope of 0.4 (assumed to represent the general relation between the [O II] and [O III] equivalent widths of radio-loud AGN as the viewing angle changes) and to separate objects with  $C \geq 0.25$  and [O III] equivalent width values below and above  $10 \text{ \AA}$  (solid line in Fig. 4). This results in a total of 25 and 93 objects in our sample being defined as weak- and strong-lined radio-loud AGN respectively.

Of the weak- and strong-lined AGN 12 (13) and 56 (37) sources respectively are part of the DXRBS (2 Jy survey). Based on DXRBS, BL Lacs (as defined by Marcha et al.) are made up of  $\sim 69$  per cent (9/13) weak- and  $\sim 31$  per cent (4/13) strong-lined radio-loud AGN. The class of radio quasars, on the other hand, contains mostly ( $\sim 98$  per cent or 46/47) strong-lined radio-loud AGN. Put differently, weak-lined radio-loud AGN include  $\sim 75$  per cent (9/12) BL Lacs,  $\sim 8$  per cent (1/12) quasars, and  $\sim 17$  per cent (2/12) radio galaxies, whereas strong-lined radio-loud AGN include  $\sim 82$  per cent (46/56) quasars,  $\sim 7$  per cent (4/56) BL Lacs, and  $\sim 11$  per cent (6/56) radio galaxies. However, because of its radio spectral index cut ( $\alpha_r \leq 0.7$ ), DXRBS selects against most radio galaxies. Therefore, considering only strongly beamed sources, i.e., sources with Ca H&K break values  $C = 0$ ,  $75^{+134}_{-49}$  per cent (3/4; errors are  $1\sigma$  uncertainties based on Poisson statistics) of the ones within the weak-lined class are BL Lacs, and  $97^{+29}_{-22}$  per cent (36/37) of the ones within the strong-lined class are quasars. This means that the overall properties of beamed weak- and strong-lined radio-loud AGN are expected to be similar to those of the previously defined BL Lac and quasar classes respectively, although no strong conclusion is possible at this time for the weak-lined sources given the small number statistics.

## 6 DISCUSSION

### 6.1 The Orientation Indicator $\alpha_{\text{oiii}}$

Our interpretation that the [O III] – [O II] equivalent width plane is suitable to disentangle orientation effects from intrinsic variations in emission line studies of radio-loud AGN was based on the assumption that the continuum optical spectral slope between the rest frame frequencies of [O II] and [O III] is indeed an orientation indicator. This can be tested using, e.g., our estimates of the narrow line region (NLR) and broad line region (BLR) luminosities, as well as measurements of the radio core dominance parameter. The BLR of radio-loud AGN, contrary to their NLR, is located much closer to the central black hole, and so can be (partially or fully) obscured by the thick, dusty torus believed to surround the nucleus in objects viewed at large angles.

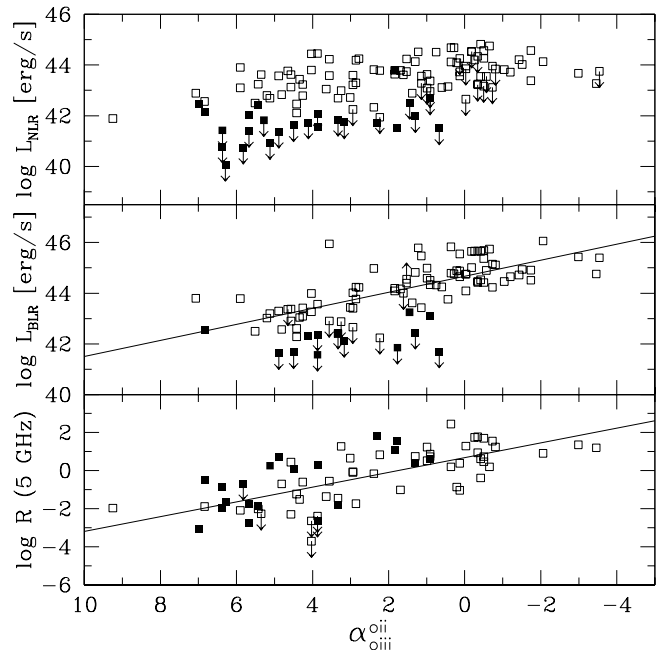


**Figure 8.** The narrow line (upper panel) and broad line region (middle panel) luminosities, and radio core dominance parameter at 5 GHz (lower panel) versus the continuum optical spectral slope (between the rest frame frequencies of [O II]  $\lambda 3727$  and [O III]  $\lambda 5007$ ) for objects from the DXRBS and 2 Jy survey. Filled and open squares denote weak- and strong-lined radio-loud AGN (as defined in our studies). Arrows indicate upper limits. The solid lines represent the observed correlations for strong-lined radio-loud AGN (middle panel) and for all sources (lower panel).

This makes the BLR luminosity, unlike the NLR luminosity, aspect dependent. Then, if  $\alpha_{\text{oiii}}$  is indeed an orientation indicator we expect it to correlate with the *anisotropic* BLR but not with the *isotropic* NLR luminosity. Similarly, we expect  $\alpha_{\text{oiii}}$  to correlate with the radio core dominance parameter  $R$  (defined as the ratio between the core and extended radio flux), which is assumed to be a suitable indicator of orientation for radio-loud AGN.

In Fig. 8 we plot the BLR (middle panel) and NLR luminosities (upper panel) versus  $\alpha_{\text{oiii}}$  for our sample of weak- (filled squares) and strong-lined radio-loud AGN (open squares). We have detected broad emission lines only for objects with Ca H&K break values  $C \lesssim 0.35$  (with the exception of 2Jy 1514+07, which has a narrow H $\alpha$  emission line with broad wings; however, its Ca break has a large error,  $C = 0.6 \pm 0.5$ ). Therefore, only these are included in Fig. 8, middle panel, and we have assumed that this is the maximum Ca H&K break value (i.e., the maximum viewing angle) for which we can expect to observe broad emission lines in the object’s spectrum. (Note that this value turns out to be the same as the one inferred by Landt et al. (2002) to be appropriate to separate core- and lobe-dominated low-luminosity radio-loud AGN). We have then derived non-detection limits on the BLR luminosity (as described in Section 3) only for objects with  $C \leq 0.35$ .

The NLR luminosity has been considered an upper limit if both the [O II] and [O III] emission lines were absent (17 objects) and also if only the [O II] emission line could not be detected (16 objects).

Indeed, for our sample of strong-lined radio-loud AGN we find a strong ( $P > 99.9$  per cent) correlation between the BLR luminosity and  $\alpha_{\text{OIII}}^{\text{OII}}$  (solid line in Fig. 8, middle panel), which remains significant even if the common redshift dependence is excluded. On the other hand, no significant ( $P = 91.1$  per cent) correlation is present between the NLR luminosity and  $\alpha_{\text{OIII}}^{\text{OII}}$  once the common redshift dependence is excluded. We have used here the algorithms for partial correlation analysis for censored data developed by Akritas & Siebert (1996). Note that a redshift dependence of  $\alpha_{\text{OIII}}^{\text{OII}}$  is expected if this is indeed a beaming indicator.<sup>2</sup> Owing to the large number of upper limits a similar analysis is not possible for our sample of weak-lined AGN.

In Fig. 8, lower panel, we plot the radio core dominance parameter at 5 GHz versus  $\alpha_{\text{OIII}}^{\text{OII}}$  for part (70/118) of our sample of weak- and strong-lined AGN. Radio core dominance parameters for 2 Jy sources were taken from Morganti et al. (1997) and for southern DXRBS sources calculated from our ATCA measurements (Bignall et al., in prep.). We note that our ATCA observations were conducted in snapshot mode which might have missed extended flux, and, therefore, the DXRBS radio core dominance values are actually upper limits to the true values. We have converted all values to a rest frame frequency of 5 GHz assuming radio spectral indices of  $\alpha_r = 0$  and 0.8 for the core and extended emission respectively. The radio core dominance parameter strongly ( $P > 99.9\%$ ) correlates with  $\alpha_{\text{OIII}}^{\text{OII}}$ , which further supports its use as a statistical orientation indicator. In this respect, we note that the composites shown in Fig. 5 are very similar to the ones presented by Baker & Hunstead (1995) for a sample of quasars selected from the Molongolo survey and grouped by  $R$ . The trends observed with increasing  $R$  are similar to the ones observed with decreasing Ca H&K break value (i.e., decreasing  $\alpha_{\text{OIII}}^{\text{OII}}$ ), namely a flattening of the continuum emission, markedly stronger appearance of the Balmer continuum, and a decrease of the [O II] and [O III] equivalent widths. This confirms in particular our interpretation that the upper and lower composites for sources with  $C = 0$  represent radio-loud AGN viewed at smaller and larger angles with respect to the line of sight. These are similar to their composites for sources with  $R \geq 0.1$  and  $R < 0.1$  respectively.

Baker (1997), however, concluded that the main cause for the flattening of the continuum of quasars at small viewing angles was a decreased obscuration by the putative circumnuclear dusty torus. In other words, the larger the viewing angle, the more the continuum was steepened by dust extinction. In support of this interpretation Baker (1997) quoted the strong correlation observed between the  $H\alpha/H\beta$  emission line ratios and optical spectral index. The amount

<sup>2</sup> In a radio flux-limited sample sources seen at smaller angles will be more strongly beamed and will then have higher powers, which will result in them being detected at redshifts higher than sources seen at larger angles.

of dust extinction predicted by this correlation seemed to explain the observed decrease in [O II] and [O III] equivalent widths with  $R$  and the observed range of optical spectral slopes. An orientation-dependent obscuration as the primary cause for the change of the optical continuum slopes of radio-loud quasars with viewing angle, however, is ruled out by the fact that we observe this trend with decreasing Ca H&K break value. The large Ca H&K break values typical for the host galaxies of radio-loud AGN, which generally have 'red' spectra, are decreased at small viewing angles by emission from the additional components jet and Balmer continuum, which typically have 'blue' spectra. Therefore, the observed change of the optical spectral slopes of radio-loud AGN with viewing angle can be fully explained by their (expected) main components dominating the continuum at different orientations. On the other hand, although we believe that dust extinction is not the dominant parameter governing the continuum shape of radio-loud AGN, it might play a role in the observed Balmer decrement decrease. In fact, we have measurements on both  $H\alpha$  and  $H\beta$  emission lines for 14 objects from the sample plotted in Fig. 4 and we find for these, similar to Baker (1997), a significant ( $P = 99.1$  per cent) anticorrelation between the  $H\alpha/H\beta$  emission line and  $\alpha_{\text{OIII}}^{\text{OII}}$ .

## 6.2 The Continuity Between Blazar Subclasses

Scarpa & Falomo (1997) investigated if BL Lacs and high-polarization quasars (HPQ) had different intrinsic emission line luminosities considering data for the broad emission line Mg II  $\lambda 2798$  for a sample of 34 sources. Their sample included 10 BL Lacs and 18 HPQ selected from the literature, but newly observed by these authors, as well as 6 BL Lacs from the 1 Jy sample of Stickel et al. (1993). Only sources with detected Mg II emission lines were considered. The approach Scarpa and Falomo chose to address the problem was to plot the logarithmic line luminosity versus continuum luminosity below the line (see their Fig. 10). In such a plot lines of constant equivalent width form diagonals with a slope of one. By plotting also the line of constant equivalent width of  $5 \text{ \AA}$  (the dividing value between BL Lacs and quasars at the time) their plot showed that the transition between BL Lacs and HPQ was continuous. Based on this, these authors argued that from the point of view of emission line strengths it was not necessary to invoke two different populations of blazars.

In Fig. 9, left panel, we show a plot similar to that of Scarpa and Falomo for our sample of weak- (filled squares) and strong-lined radio-loud AGN (open squares) for the [O III]  $\lambda 5007$  emission line. The solid line indicates a constant equivalent width of  $5 \text{ \AA}$ . In Fig. 9, right panel, we have plotted for the same objects the [O III] rest frame equivalent width versus  $\alpha_{\text{OIII}}^{\text{OII}}$ . These plots illustrate two important points. First, *given a bimodal distribution for an emission line*, which is the only physical justification for a separation of radio-loud AGN based on emission line strength, the equivalent width separating the two classes will depend on orientation. A constant equivalent width value is not suitable for this purpose. In this respect, Fig. 9, right panel,



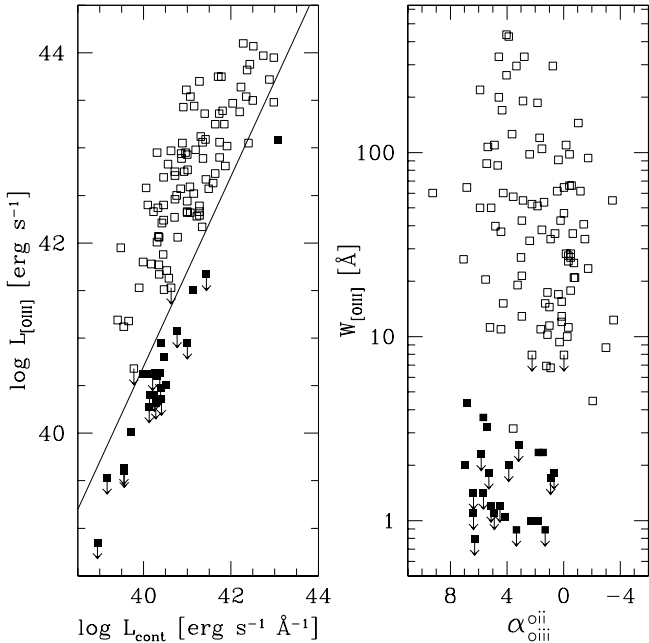


**Figure 9.** **Left panel:** The [O III]  $\lambda 5007$  line luminosity versus the continuum luminosity underneath the line for sources from the DXRBS and 2 Jy survey. Filled and open squares indicate weak- and strong-lined radio-loud AGN respectively. Arrows indicate upper limits. The solid line indicates a constant equivalent width of 5 Å. This plot is similar to Fig. 10 of Scarpa and Falomo (1997). **Right panel:** The [O III]  $\lambda 5007$  rest frame equivalent width versus the continuum optical spectral slope (between the rest frame frequencies of [O II]  $\lambda 3727$  and [O III]  $\lambda 5007$ ) for objects from the DXRBS and 2 Jy survey. Symbols as in left panel. Note that both panels include the same objects. See text for details.

illustrates clearly the [O III] bimodality (thus the need for two classes of radio-loud AGN) as well as the dependence of the dividing equivalent width value on orientation, of which  $\alpha_{\text{OIII}}^{\text{OII}}$  is a suitable statistical indicator. Second, a comparison between the plots in the left and right panel of Fig. 9 shows that even when a bimodality is present for an emission line of radio-loud AGN this will not be clearly evident in a plot of line luminosity versus continuum luminosity. Such a plot does not allow one to disentangle orientation effects from intrinsic variations, a step which is, however, crucial in studies involving emission lines of radio-loud AGN.

### 6.3 The Classification of Radio-Loud AGN

This work together with our earlier paper (Landt et al. 2002) represent a complete physical revision of the current classification scheme for blazars proposed by Marchã et al. (1996).

There have been previous attempts to separate radio-loud AGN, in particular radio galaxies, based on their [O III] emission line strengths. However, in all these studies the separation value was chosen rather arbitrarily. For example, Laing et al. (1994) divided their sample of FR

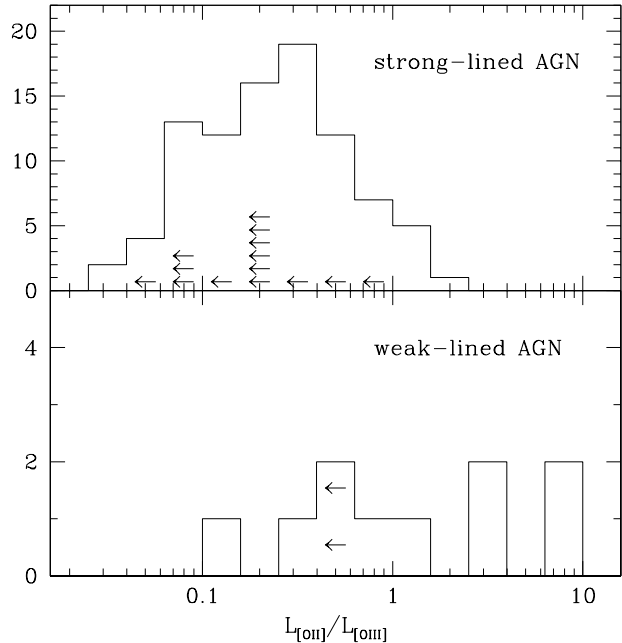


**Figure 10.** The distribution of the [O II]  $\lambda 3727$  to [O III]  $\lambda 5007$  line luminosity ratio for weak- (lower panel) and strong-lined radio-loud AGN (upper panel) from the DXRBS and 2 Jy surveys. Arrows indicate upper limits on the [O II] line luminosity.

II radio sources from the 3CR survey into low- and high-excitation objects, which they defined to have [O III] equivalent widths below and above 3 Å respectively, with the latter required to have also emission line ratios [O III]/ $H\alpha$  (narrow)  $> 0.2$ . Similarly, Jackson & Rawlings (1997) classified radio galaxies in their subsample of 3CR and 3CRR radio sources as low- (LEG) and high-ionization narrow-line radio galaxies (HEG) if they had [O III] equivalent widths below and above 10 Å respectively. Radio galaxies with emission line ratios [O II]/[O III]  $> 1$  also fell in the former category. Tadhunter et al. (1998) distinguished in their sample of radio sources from the 2 Jy survey between narrow- (NLRG) and weak-line radio galaxies (WLRG), the latter defined as sources with their spectra dominated by stellar absorption features from the host galaxy and [O III] emission lines weaker than 10 Å.

In this respect, we note that the separation value of  $W_{[\text{O III}]} = 10 \text{ \AA}$  of Jackson & Rawlings (1997) and Tadhunter et al. (1998), although selected rather arbitrarily, coincides with the intersection point of the two best-fit Gaussians to the [O III] equivalent width distribution of sources with  $C \geq 0.25$  plotted in Fig. 4 and so roughly with our separation of weak- and strong-lined radio galaxies (see Section 5.3). However, our classification is not equivalent to the separation of Jackson & Rawlings (1997) into low- and high-ionization radio-loud AGN. Fig. 10 plots the [O II]/[O III] emission line ratio distributions for our weak- (lower panel) and strong-lined sources (upper panel), excluding sources with upper limits on both their [O II] and [O III] emission line luminosities (10/25 and 91/93 objects

respectively). From this we see that, whereas most (85/91 or 93.4 per cent) strong-lined AGN have ratios  $[\text{O II}]/[\text{O III}] < 1$  and could be classified as high-ionization sources, the class of weak-lined AGN appears to be heterogeneous with equal number of sources having  $[\text{O II}]/[\text{O III}] < 1$  and  $> 1$ .

Our new classification scheme, namely the  $[\text{O III}] - [\text{O II}]$  equivalent width plane, is easily applicable to sources with  $z \lesssim 0.8$ , for which the optical spectrum (typically spanning the wavelength range 3500 – 9000 Å) allows the detection of both the  $[\text{O II}]$  and  $[\text{O III}]$  emission lines. In this redshift range, actually, all one needs in most cases is  $[\text{O III}]$ . Fig. 9, in fact, shows that all sources with  $W_{[\text{O III}]} > 6$  Å are of the strong-lined type, while all sources with  $W_{[\text{O III}]} < 3$  Å are of the weak-lined type. Only when  $W_{[\text{O III}]}$  is in between these two values one needs  $[\text{O II}]$  as well. For sources at higher redshifts, however, infrared spectra are required. In this respect note that even the classification scheme proposed by Marchã et al. (1996) requires infrared spectra for sources with redshifts  $z \gtrsim 1.2$ , for which the Ca H&K break is located outside the optical window.

Our new classification scheme is based on emission line equivalent width and, therefore, in the case of radio galaxies (objects with  $C \geq 0.25$ ) where the host galaxy dominates the continuum, it is expected to depend also on spectroscopic constraints such as a final slit width. A narrow slit will limit the fraction of galaxy light included, and will lead to an overestimation of the equivalent widths of these sources at low redshifts. This could introduce a bias against low-redshift weak-lined AGN with  $C \geq 0.25$ , since these will be ‘misclassified’ as strong-lined AGN. However, simulations show that this kind of observational constraints are expected to affect our classification scheme only for very nearby radio galaxies. Assuming an elliptical host galaxy with a de Vaucouleurs surface brightness profile and a half-light radius of 10 kpc (e.g., Pagani et al. 2003) we get that for sources at redshifts  $z \lesssim 0.07$  and  $z \lesssim 0.03$  the equivalent width will be overestimated by factors  $\gtrsim 5$  and  $\gtrsim 10$  respectively compared to the value measured at large redshifts. The effects due to a difference in slit width are less severe. For example, we expect the equivalent widths to be overestimated only by a factor of  $\sim 2$  if one uses a slit width of  $1''$  instead of  $5''$ .

## 7 SUMMARY AND CONCLUSIONS

We have used radio-loud AGN from the DXRBS and 2 Jy survey to readdress the separation of blazars into BL Lacs and FSRQ as well as the general classification of radio-loud AGN based on their emission lines. In this respect, this work represents a physical revision of the present classification scheme proposed by Marchã et al. (1996). Our main results can be summarized as follows:

(i) We have argued that a physically justified separation of blazars based on emission line strength requires the presence of a bimodal distribution for any of the *narrow* emission lines inherent to the entire class of radio-loud AGN. In our studies we have considered the equivalent width distributions of the narrow emission lines  $[\text{O II}] \lambda 3727$  and  $[\text{O III}] \lambda 5007$  for  $\sim 100$  blazars and radio galaxies from the

DXRBS and 2 Jy survey. We have found a bimodal distribution for the  $[\text{O III}]$  emission line.

(ii) We have shown that all radio-loud AGN can be separated unambiguously into sources with *intrinsically* weak and strong  $[\text{O III}]$  emission lines (dubbed weak- and strong-lined radio-loud AGN respectively) using an  $[\text{O III}] - [\text{O II}]$  equivalent width plane. This plane is suitable to disentangle orientation effects and intrinsic variations in radio-loud AGN. In most cases our classification scheme requires only  $[\text{O III}]$ , since all sources with  $W_{[\text{O III}]} > 6$  Å are of the strong-lined type, while all sources with  $W_{[\text{O III}]} < 3$  Å are of the weak-lined type.

(iii) We have presented composite spectra that illustrate that different components dominate the continuum emission of radio-loud AGN at different orientations. In particular, at shorter optical wavelengths the continuum emission is dominated by the host galaxy, jet emission and Balmer continuum for sources viewed at large, intermediate, and small angles respectively.

(iv) Based on DXRBS, the strongly beamed sources (i.e., sources with Ca H&K break values of  $C = 0$ ) of the weak-lined class include  $\sim 75$  per cent BL Lacs, whereas those of the strong-lined class are mostly ( $\sim 97$  per cent) quasars. This means that the overall properties of beamed weak- and strong-lined radio-loud AGN are expected to be similar to those of BL Lacs and quasars respectively.

We note that our classification scheme is somewhat dependent on observational constraints in the case of radio galaxies and weakly beamed sources, due to their strong host galaxy component. However, simulations show that this affects only relatively low redshift ( $z \lesssim 0.1$ ) sources.

A bimodal equivalent width distribution for an emission line of radio-loud AGN has not been reported so far. Therefore, this important result needs further testing. This can be done, e.g., using the MRC/1 Jy radio sample, which contains a large number of sources ( $\sim 550$  objects) with uniform spectroscopic observations, as well as current ongoing surveys, such as, e.g., RGB (Laurent-Muehleisen et al. 1998, 1999), REX (Caccianiga et al. 1999, 2000), and the low-redshift selected CLASS blazar sample (Marchã et al. 2001; Caccianiga et al. 2002). In a subsequent paper we plan to investigate the physical differences between weak- and strong-lined radio-loud AGN using their emission line measurements as well as information on their radio, optical and X-ray luminosities.

## ACKNOWLEDGEMENTS

We thank Clive Tadhunter for providing the spectra of radio sources from the 2 Jy survey in electronic format, and the anonymous referee for suggestions which led to major improvements of our manuscript. H.L. acknowledges financial support from the STScI DDRF grants D0001.82260 and D0001.82299. E.P. acknowledges support from NASA grants NAG5-10109 and NAG5-9995, as well as NAG5-9997 (LTSA).

**REFERENCES**

- Akritas M. G., Siebert J., 1996, *MNRAS*, 278, 919  
 Ashman K. M., Bird C. M., Zepf S. E., 1994, *AJ*, 108, 2348  
 Baker J. C., 1997, *MNRAS*, 286, 23  
 Baker J. C., Hunstead R. W., 1995, *ApJ*, 452, L95  
 Baldwin J. A., Wampler E. J., Gaskell C. M., 1989, *ApJ*, 338, 630  
 Blandford R. D., Rees M. J., 1978, in Wolfe A. M., ed, *Pittsburgh Conference on BL Lac Objects*. University of Pittsburgh, Pittsburgh, p. 328  
 Caccianiga A., Maccacaro T., Wolter A., Della Ceca R., Gioia I. M., 1999, *ApJ*, 513, 51  
 Caccianiga A., Maccacaro T., Wolter A., Della Ceca R., Gioia I. M., 2000, *A&AS*, 144, 247  
 Caccianiga A., Marchà M. J., Antón S., Mack K.-H., Neeser M. J., 2002, *MNRAS*, 329, 877  
 Celotti A., Padovani P., Ghisellini G., 1997, *MNRAS*, 286, 415  
 Chiaberge M., Capetti A., Celotti A., 1999, *A&A*, 349, 77  
 Chiaberge M., Capetti A., Celotti A., 2002, *A&A*, 394, 791  
 Czerny B., Elvis M., 1987, *ApJ*, 321, 305  
 D'Elia V., Padovani P., Landt H., 2003, *MNRAS*, 339, 1081  
 Dressler A., Sheckman S. A., 1987, *AJ*, 94, 899  
 Fanaroff B. L., Riley J. M., 1974, *MNRAS*, 167, 31  
 Filippenko A. V., 1982, *PASP*, 94, 715  
 Francis P. J., Hewett P. C., Foltz C. B., Chaffee F. H., Weymann R. J., Morris S. L., 1991, *ApJ*, 373, 465  
 Gaskell C. M., Shields G. A., Wampler E. J., 1981, *ApJ*, 249, 443  
 Giommi P., Menna M. T., Padovani P., 1999, *MNRAS*, 310, 465  
 Hes R., Barthel P. D., Fosbury R. A. E., 1996, *A&A*, 313, 423  
 Isobe T., Feigelson E. D., Nelson P. I., 1986, *ApJ*, 306, 490  
 Jackson N., Browne I. W. A., 1991, *MNRAS*, 250, 414  
 Jackson N., Eracleous M., 1995, *MNRAS*, 276, 1409  
 Jackson N., Rawlings S., 1997, *MNRAS*, 286, 241  
 Koratkar A., Blaes O., 1999, *PASP*, 111, 1  
 Laing R. A., Jenkins C. R., Wall J. V., Unger S. W., 1994, in Bicknell G. V., Dopita M. A., Quinn P. J., ed, *The First Stromlo Symposium: The Physics of Active Galaxies*. A.S.P., San Francisco, p. 201  
 Landt H., Padovani P., Giommi P., 2002, *MNRAS*, 336, 945  
 Landt H., Padovani P., Perlman E. S., Giommi P., Bignall H., Tzioumis A., 2001, *MNRAS*, 323, 757  
 Laurent-Muehleisen S. A., Kollgaard R., Feigelson E. D., Brinkmann W., Siebert J., 1999, *ApJ*, 525, 127  
 Laurent-Muehleisen S. A., Kollgaard R. I., Ciardullo R., Feigelson E. D., Brinkmann W., Siebert J., 1998, *ApJS*, 118, 127  
 Lawrence C. R., Zucker J. R., Readhead A. C. S., Unwin S. C., Pearson T. J., Xu W., 1996, *ApJS*, 107, 541  
 Malkan M. A., Sargent W. L. W., 1982, *ApJ*, 254, 22  
 Maoz D. et al., 1993, *ApJ*, 404, 576  
 Marchà M. J., Caccianiga A., Browne I. W. A., Jackson N., 2001, *MNRAS*, 326, 1455  
 Marchà M. J. M., Browne I. W. A., Impey C. D., Smith P. S., 1996, *MNRAS*, 281, 425  
 Morganti R., Oosterloo T. A., Reynolds J. E., Tadhunter C. N., Migenes V., 1997, *MNRAS*, 284, 541  
 Padovani P., Urry C. M., 1990, *ApJ*, 356, 75  
 Padovani P., Urry C. M., 1991, *ApJ*, 368, 373  
 Padovani P., Urry C. M., 1992, *ApJ*, 387, 449  
 Pagani C., Falomo R., Treves A., 2003, *ApJ*, 596, 830  
 Perlman E. S., Padovani P., Giommi P., Sambruna R., Jones L. R., Tzioumis A., Reynolds J., 1998, *AJ*, 115, 1253  
 Rawlings S., Saunders R., 1991, *Nature*, 349, 138  
 Richstone D. O., Schmidt M., 1980, *ApJ*, 235, 361  
 Saunders R., Baldwin J. E., Rawlings S., Warner P. J., Miller L., 1989, *MNRAS*, 238, 777  
 Scarpa R., Falomo R., 1997, *A&A*, 325, 109  
 Stickel M., Fried J. W., Kühr H., 1989, *A&AS*, 80, 103  
 Stickel M., Fried J. W., Kühr H., 1993, *A&AS*, 98, 393  
 Stickel M., Kühr H., 1993, *A&AS*, 100, 395  
 Stickel M., Kühr H., Fried J. W., 1993, *A&AS*, 97, 483  
 Stickel M., Padovani P., Urry C. M., Fried J. W., Kühr H., 1991, *ApJ*, 374, 431  
 Stocke J. T., Morris S. L., Gioia I. M., Maccacaro T., Schild R., Wolter A., Fleming T. A., Henry J. P., 1991, *ApJS*, 76, 813  
 Strittmatter P. A., Serkowski K., Carswell R., Stein W. A., Merrill K. M., Burbidge E. M., 1972, *ApJ*, 175, L7  
 Tadhunter C. N., Morganti R., di Serego-Alighieri S., Fosbury R. A. E., Danziger I. J., 1993, *MNRAS*, 263, 999  
 Tadhunter C. N., Morganti R., Robinson A., Dickson R., Villar-Martin M., Fosbury R. A. E., 1998, *MNRAS*, 298, 1035  
 Urry C. M., Padovani P., 1995, *PASP*, 107, 803  
 Urry C. M., Padovani P., Stickel M., 1991, *ApJ*, 382, 501  
 White N. E., Giommi P., Angelini L., 1995, <http://wgacat.gsfc.nasa.gov/wgacat/wgacat.html>  
 Wilkes B. J., 1986, *MNRAS*, 218, 331  
 Wills B. J., Netzer H., Wills D., 1985, *ApJ*, 288, 94  
 Wurtz R., Stocke J. T., Yee H. K. C., 1996, *ApJS*, 103, 109